N. Mayer

(NASA-CR-152127) THEORETICAL STUDY OF HULL-ROTOR AERODYNAMIC INTERFERENCE ON SEMIBUOYANT VEHICLES Technical Report, 14 Feb. - 7 Dec. 1977 (Neilsen Engineering and Research, Inc.) 97 p HC A05/MF A01 CSCL 01A G3/02

N81-15981

Unclas
41210

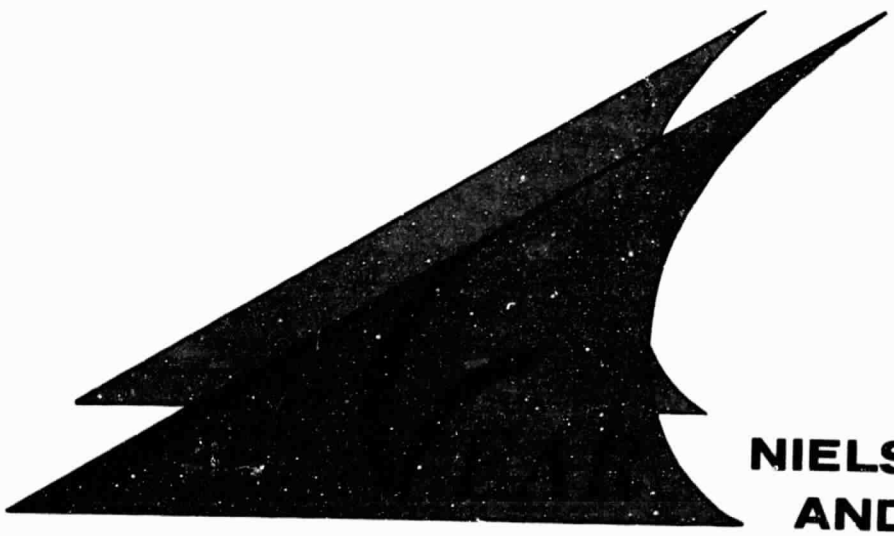

NIELSEN ENGINEERING AND RESEARCH, INC.

OFFICES: 510 CLYDE AVENUE / MOUNTAIN VIEW, CALIFORNIA 94043 / TELEPHONE (415) 968-9457

NASA CR-152127

THEORETICAL STUDY OF HULL-ROTOR AERODYNAMIC INTERFERENCE ON SEMIBUOYANT VEHICLES

by

S. B. Spangler and C. A. Smith

NEAR TR 159

April 1978

Prepared under Contract No. NAS2-9512

by

NIELSEN ENGINEERING & RESEARCH, INC.
Mountain View, California 94043

for

AMES RESEARCH CENTER
National Aeronautics and Space Administration
Moffett Field, California 94035

TABLE OF CONTENTS

LIST OF ILLUSTRATIONS

Figure

LIST OF ILLUSTRATIONS (Concluded)

Figure

THEORETICAL STUDY OF HULL-ROTOR AERODYNAMIC INTERFERENCE ON SEMIBUOYANT VEHICLES

by

S. B. Spangler and C. A. Smith
Nielsen Engineering & Research, Inc.

SUMMARY

Analytical methods have been developed to predict the pressure distribution and overall loads on the hulls of airships which have close coupled, relatively large and/or high disk loading propulsors for attitude control, station keeping, and partial support of total weight as well as provision of thrust in cruise. The methods comprise a surface-singularity, potential-flow model for the hull and lifting surfaces (such as tails) and a rotor model which calculates the velocity induced by the rotor and its wake at points adjacent to the wake. Use of these two models provides an inviscid pressure distribution on the hull with rotor interference. A boundary-layer separation prediction method is used to locate separation on the hull, and a wake pressure is imposed on the separated region for purposes of calculating hull loads.

A number of calculations were made to investigate and illustrate the nature of hull-rotor interactions. One basic configuration was examined for hull alone, rotor alone, and hull-rotor combinations in hover, axial flow, and crossflow (β=90°) in and out of ground effect. Comparison with the limited data available on this configuration showed generally good agreement on the hull alone, including cases of large separated flow on the hull, and the rotor alone. The predicted loads on the hull-rotor combinations appear reasonable and consistent, but differ from measured values in sign of the normal force. The quality and quantity of the data are insufficient to establish the source of the differences.

INTRODUCTION

Historically, airships have been rather lightly powered and have used their propulsion systems to overcome drag in cruise. The airships were operated close to the neutrally buoyant condition, and aerodynamic lift on the hull was used to make up differences between buoyant force and weight.

More recently, interest has been generated in airships which have a considerably higher installed thrust capability relative to vehicle weight. Recent NASA-sponsored work has identified the Heavy Lift Airship (HLA) and a passenger feeder liner as promising applications for modern airship technology.[1,2] These vehicles characteristically have relatively large rotors or propellers, which can be mounted at various locations on the hull and which are expected to produce thrust for attitude control, station keeping, and partial support of the total weight as well as for overcoming drag in cruise. Because of the higher thrust levels produced and the tilting capability in these propulsors, there is the possibility of large interactions that can occur between the rotor wakes and the hull, which can produce either favorable or unfavorable interference loads on the vehicle. Due to the magnitudes of these effects, it is necessary to know their characteristics before the design of a vehicle is finalized and to use their characteristics to determine the control power available, the capability to station-keep in a wind, and the approach to the control system design.

Since the problem is relatively new, there are no existing analytical methods to predict interference effects of this nature and very little appropriate data. Perhaps the most applicable data source is results of tests conducted under Goodyear Aerospace Corporation sponsorship at the Ames Research Center by Nielsen Engineering & Research on a 1/79th scale model of the Heavy Lift Airship vehicle being studied by GAC under their NASA contract.[3]

The objective of the program described in this report is to develop a theoretical method for predicting hull loads with rotor interference on semibuoyant airships. The method is to be general in the sense that it can be applied to a variety of hull shapes (not necessarily axisymmetric) with rotors, of a wide range of disk loading, located adjacent to the hull. In addition, it is necessary that the method be applicable to a vehicle operating near the ground and to vehicle attitudes relative to the wind direction such that substantial areas of separated flow may occur on the hull.

This report describes the development of the methods and results obtained with the method on typical configurations. Included are comparisons with experimental data whenever possible.

NOMENCLATURE

b	Number of rotor blades
$C_{M_x}, C_{M_y}, C_{M_z}$	Moment coefficients on hull, nondimensionalized by $q_\infty \Psi$
C_p	Pressure coefficient, based on q_∞
C_p'	Modified pressure coefficient, based on U_m, equation 16
C_T	Rotor thrust coefficient, $T/\rho_\infty (\Omega R)^2 \pi R^2$
C_X, C_Y, C_Z	Force coefficients on hull, nondimensionalized by $q_\infty \Psi^{2/3}$
D	hull maximum diameter
$F(s)$	Empirical parameter in separation criterion
H	Height of hull geometric center above ground
L	Coordinate along axis of rotor wake
M_T	Rotor thrust moment, or moment about the flapping hinge due to the thrust
M_x, M_y, M_z	Moments on hull about x, y, and z axes, respectively, positive "right wing down", nose up, and nose right, respectively (fig. 1)
n	Coordinate normal to hull surface
q_∞	Free stream dynamic pressure
r	Radial coordinate
$\vec{r}$	Vectorial distance from origin to a field point
R	Rotor radius
R_c	Distance from point on rotor disk to field point
Re_D	Free stream Reynolds number, based on hull maximum diameter
Re_s	Reynolds number based on distance along hull surface from virtual origin
R_p	Distance from rotor center to field point
s	Coordinate along hull surface in a y,z plane
s'	Distance along hull surface from stagnation point to location of virtual origin in separation criteria
s_m	Distance along hull surface from stagnation point to location of maximum velocity
$\vec{s}$	Vector from rotor center to point on wake

NOMENCLATURE (continued)

S_R	Rotor disk area
T	Rotor thrust
u,v,w	Velocity components in x,y,z directions, respectively
U_e	Magnitude of inviscid (or boundary layer edge) velocity
U_m	Magnitude of maximum inviscid velocity on hull
U_T	Tangential component of relative velocity at rotor blade element
U_a,V_a,W_a	Components of rotor-induced velocity due to axial vorticity
U_c,V_c,W_c	Components of rotor-induced velocity due to circumferential vorticity
U_r,V_r,W_r	Components of rotor-induced velocity due to radial vorticity
U_R,V_R,W_R	Components of rotor-induced velocity due to root vorticity
$\forall$	Hull volume
V	Total velocity
V_j	Rotor wake velocity at plane of rotor (from momentum theory)
$\vec{V}_R$	Rotor-induced velocity due to root vorticity
V_∞	Free stream velocity
x,y,z	Coordinates in a body axis system centered at the body geometric center; x forward, y to starboard and z downward (fig. 1)
X,Y,Z	Forces on hull along the x,y, and z directions, respectively
x_Q,y_Q,z_Q	Coordinates of rotor center in hull coordinate system (fig. 1)
x_R,y_R,z_R	Coordinate system with origin at center of rotor hub; x_R downstream, y_R to starboard and z_R vertically upward (fig. 1)
α	Angle of attack

NOMENCLATURE (concluded)

β	Angle of sideslip
$\gamma_1, \gamma_2, \gamma_3, \gamma_4$	Rotor blade circulation strengths due to, respectively, root vorticity, ring vorticity, axial vorticity, and radial vorticity (fig. 2)
Γ	Total circulation on rotor blade
Γ_0	Part of blade circulation independent of azimuth
Γ_1	Portion of blade circulation that varies with the azimuthal angle ψ
Γ_a	Circulation strength of the rotor blade axial vorticity
Γ_c	Circulation strength of the rotor blade circumferential vorticity
Γ_R	Circulation strength of the rotor blade root vorticity
Γ_v	Strength of a vortex filament
λ	Rotor inflow ratio, nondimensional component of velocity perpendicular to rotor disk, $\frac{V_\infty \sin \alpha + V_i}{\Omega R}$
μ	Rotor tip-speed ratio, nondimensional component of velocity parallel to rotor disk, $\frac{V_\infty \cos \alpha}{\Omega R}$
ρ_∞	Free-stream density
σ	Surface source density distribution
ϕ	Velocity potential for disturbance velocity
Φ	Velocity potential for total velocity
χ	Rotor skew angle, figure 1
ψ	Azimuthal angle around the rotor disk, figure 1
Ω	Rotor rotational speed
ω_a	Magnitude of rotor axial vorticity
ω_c	Magnitude of rotor circumferential vorticity
$\vec{\omega}_{ToT}$	Rotor tip vortex

OVERALL APPROACH

The overall approach to the development of a hull-rotor interference model is to use potential flow methods to describe the flow over a hull and the flow field induced by a rotor, combine these two methods to calculate an inviscid hull pressure distribution with hull-rotor interference, and modify this pressure distribution according to predicted flow separation and wake pressure calculations. Thus, two potential flow models, a method for predicting boundary layer separation, and a wake pressure model are required.

The hull potential flow method used is the incompressible lifting model of reference 4. This method, and the resulting computer program (reference 5), calculates the inviscid pressure distribution on an arbitrary nonlifting body, a lifting wing, or a body-wing combination. The program places the configuration in a uniform onset flow and uses various types of singularities, depending on the surface being modeled. It has a provision for symmetry planes to reduce computation time. For purposes of this investigation, the program can be made to model an airship hull of arbitrary shape, in or out of ground effect, with or without tail surfaces.

The rotor potential flow model is based on the theory developed by Heyson (refs. 6 and 7) for a rotor alone in a uniform flow. The model uses vortex filaments to represent the blade bound, trailing, and shed vorticity and calculates the strength of the vorticity distribution from the rotor thrust, advance ratio and angle of attack. The vorticity distribution can be used to calculate rotor-induced velocities in the vicinity of the rotor.

When the two models are combined, the influence of the hull on rotor thrust can be estimated, the rotor vorticity distribution calculated, the rotor wake placed in relation to the hull, and the rotor-induced velocities used as a nonuniform onset flow

added to the uniform free-stream flow to impinge on the hull. The hull-tail surface singularity distribution is then calculated in the presence of the two onset flows to obtain the inviscid pressure distribution.

Boundary-layer separation location is computed by applying empirically developed separation criteria to the hull inviscid pressure distribution. For those parts of the hull that are located downstream of separation, the inviscid pressure is replaced by a wake pressure assumed constant over the separated region at the value at separation. Loads on the hull are then computed.

The individual methods and their use in combination are described in following sections.

FLOW MODELS

Hull Potential Flow Model

General Theory.- The hull flow model determines the forces and moments acting on the hull and the pressure distribution on the hull surface by representing the hull surface by a finite number of surface source singularities. The flow field used to calculate the required strengths of these source singularities includes both the uniform free stream and the nonuniform flow induced on the hull surface by the rotor wakes.

The mathematical solution to this problem proceeds in the following manner. At any point the fluid velocity is assumed to satisfy Laplace's equation which can be expressed as

$$\nabla^2 \Phi = 0 \tag{1}$$

where

$$\vec{V} = \text{grad } \Phi \tag{2}$$

In addition the velocity is subject to two boundary conditions. The first is that the normal velocity component on the surface of body is zero and the other is that the velocity approaches that of the free stream at infinity. Symbolically, these boundary conditions are written

$$\left.\frac{\partial \Phi}{\partial n}\right|_{\text{surface}} = 0 \tag{3}$$

$$\lim_{\vec{r}\to\infty} (\text{grad } \Phi) = \vec{V}_\infty \tag{4}$$

Divide the velocity potential into a part due to the uniform free stream and a part due to the disturbance velocity such that

$$\Phi = \Phi_\infty + \phi \tag{5}$$

where

$$\text{grad } \phi = \vec{V}_\infty \tag{6}$$

The governing equation and boundary conditions then become

$$\nabla^2 \phi = 0 \tag{7}$$

$$\left.\frac{\partial \phi}{\partial n}\right|_{\text{surface}} = \vec{n} \cdot \vec{V}_{\infty\ \text{surface}} \tag{8}$$

$$\lim_{\vec{r}\to\infty} (\text{grad } \phi) = 0 \tag{9}$$

Use is now made of the result shown in reference 8 that the body surface can be covered by a surface source density distribution σ. In terms of this source distribution the governing equation and boundary conditions given by equations (7), (8), and (9) reduce to the single equation

$$2\pi\sigma(p) - \oiint_{\text{surface}} \frac{\partial}{\partial n}\left[\frac{1}{|\vec{r}_p - \vec{r}_q|}\right]\sigma(q)\,dS = -\vec{n}(p)\cdot\vec{V}_\infty \qquad (10)$$

where points p and q are on the surface of the body and dS is an elemental surface area of the body. This equation is a two-dimensional Fredholm integral equation of the second kind over the surface.

Solution.- There are several methods to solve equation (10). The one chosen for the present application is that developed at Douglas by Hess and Smith and reported in references 4 and 9. This method consists of approximating the body surface by a large number of plane quadrilaterals. The source density is taken to be constant over each quadrilateral or panel and one point is specified (control point) on each panel where equation (10) is required to hold. This reduces the integral equation to a set of linear equations equal to the number of panels used to represent the body surface.

The resulting set of linear equations is used to determine the source densities. Once this is determined the flow velocities at the control points are evaluated by calculating the contribution of each of the source elements and adding the components of the free stream. Finally, the pressure distribution over the surface is determined with the Bernoulli pressure equation, i.e.

$$C_p = 1 - \left(\frac{V}{V_\infty}\right)^2 \qquad (11)$$

Once the pressure distribution over the surface is determined the forces and moments are evaluated by assuming the pressure at a panel to act on the surface area of that panel to provide a force along the normal to the panel at the control point and summing over the body surface. The details of the computation and program are presented in reference 5.

The potential flow computer program developed at Douglas was modified in two ways in order to study rotor-hull configurations. The first addition was to compute the velocity at each control point induced by the rotor wakes and then add this velocity to the free-stream velocity to get the total onset flow. The flow model used to evaluate these rotor-wake-induced velocities is described in the following section. The second modification takes the inviscid pressure distribution determined by equation (11) and uses it to calculate the point of turbulent separation. The details of the flow separation model are described in a subsequent section. All panels downstream of the separation point are then assigned a pressure equal to the pressure at separation. This modified pressure distribution is then used to calculate forces and moments.

Lifting Surface Model

The Douglas program is capable of representing body-lifting surface combinations in addition to bodies alone. In the present application, this capability provides a means of modeling tail surfaces on airship hulls, for example. The general approach is similar to that for the body alone.

The lifting surface is divided into an arrangement of panels on the pressure and suction surfaces. A surface source distribution on both surfaces is used to model the thickness. The lift is modeled by a surface vorticity distribution, which is treated as an equivalent dipole distribution for calculation purposes, and trailing vorticity. The chordwise strength distribution of the surface vorticity at a given span station is uniform, and its strength is calculated from a Kutta condition. Reference 4 gives considerable information on the method. Any lifting surface planform, thickness distribution, and camber can be modeled by the method. The lifting surface may be placed anywhere on the body surface. The junction between the body and lifting surface is

handled by extending the surface one row of panels inside the body to eliminate the discontinuity in the lifting surface vorticity representation at the junction.

Rotor Wake Model

A potential flow model of a rotor wake is required to calculate the disturbance velocity induced by that rotor at points adjacent to and outside of the wake (i.e., on the hull). Generally, the propulsors that are being considered for semibuoyant airships are low solidity devices like propellers and helicopter rotors rather than high solidity devices like turbofans. Consequently a rotor model rather than a jet model seems most appropriate for the propulsor wake.

The model chosen to represent the rotor wake is an extension of the model developed by Heyson (refs. 6 and 7). This model has the advantage of being an analytical model which represents most of the important features of the wake vorticity distribution and which is very quick to execute on a computer. The alternative is one of several numerical models which have been developed more recently and which can calculate in greater detail the rotor disk inflow distribution and velocity distribution within the wake, but at a great increase in computer time. Since the present interest is in predicting velocities outside the wake, the Heyson model is considered the best choice.

The Heyson model is shown in figure 2. The circulation along the blade is taken to be uniform in the radial direction. Thus, trailing vortices emanate from the blade tip and the blade root. The root vortex (γ_1) is a single vortex filament and lies along the wake centerline while the tip vortex forms the wake outer layer and is in the shape of a helix. The wake extends downstream to infinity along a straight centerline and the wake cross section is constant in size.

It is now assumed that the tip vortices are so closely spaced that they form a continuous cylindrical sheet of vorticity. This assumption is equivalent to assuming an infinite number of blades and constrains the analysis to determining the time-averaged induced velocities. The cylindrical vortex sheet representing the tip vortex is then divided into two components: one part being circumferential vorticity (or vortex rings) (γ_2) and the other part being axial vorticity (γ_3). Hence the tip vortex is separated into two parts, the sum of which is the strength of the tip vortex. This is shown in figure 3 taken from reference 7.

A rotating blade in forward flight will experience a change in the velocity field with a change in azimuthal position around the rotor disk. To account for this the blade circulation (and, therefore, the wake vorticity) is allowed to vary with the azimuth angle, ψ, as $\sin \psi$. Thus additional radial vorticity (γ_4) is shed from the trailing edge of the blades as a result of the changes in blade circulation. This change in circulation is continuous, so the wake cylinder is completely filled with radial vorticity of a strength proportional to the derivative of the circulation change with azimuth. The total blade circulation is, therefore, given by the relation

$$\Gamma = \Gamma_0 + \Gamma_1 \sin \psi \tag{12}$$

Further assumptions of the model are that the wake is non-contracting, is straight, and leaves the rotor disk in the presence of a free stream at an angle (skew angle) determined by momentum theory. Finally, it is assumed that the wake does not impinge on any nearby surface nor is it influenced by either nearby surfaces or a non-uniform free stream.

When determining the contribution to the induced velocity from each of the various components of vorticity, no simplifications have been made as in the original development by Heyson

(ref. 7) where the axial vorticity was assumed negligible for all but high speed forward flight.

The velocity at a point induced by a vortex filament is given by the Biot-Savart law. For a single filament this is expressed as

$$\vec{V}(\vec{r}) = -\frac{\Gamma_v}{4\pi}\int \frac{d\vec{\ell}\times(\vec{r}-\vec{s})}{|\vec{r}-\vec{s}|^3} \tag{13}$$

where Γ_v is the strength of the filament. In the present situation the induced velocity at a point is determined by the independent application of the Biot-Savart law to each of the four vortex systems in the wake. The total induced velocity is then the summation of these four contributions.

The expression for the velocity due to the root vortex can be solved directly in closed form. However, the expressions for the other three velocity contributions must be solved by numerically integrating around the rotor disk. These expressions are derived and presented in Appendix A.

The application of the method requires specification of the thrust coefficient, the rotor radius, the angular rate, the free stream velocity and its angles of attack and sideslip, and the attitude of the rotor relative to the hull. From this information, the rotor thrust and the blade circulation can be calculated assuming that the thrust produces a uniform downwash through the rotor disk in accordance with the momentum equations. Finally, the wake skew angle is calculated as the resultant direction of the vector sum of the rotor-induced downwash velocity and the horizontal and vertical components of the free-stream velocity.

HULL FLOW SEPARATION

Separation Location

The flow over the hull at all practical wind speeds will separate and change the hull pressure distribution from that predicted by potential theory. In a largely axial flow condition, separation will occur over the aft end of the hull and the presence of the rotors will have little influence on hull flow separation (unless there is a stern-mounted rotor), nor will hull flow separation have much influence on the rotors. In a largely crossflow condition, separation occurs along the length of the hull, and the hull flow separation - rotor performance interaction can be significant. A flow separation model was incorporated in the hull flow model which, in principle, can treat both the axial and crossflow types of separation. In practice, the method was implemented in the computer program only in the crossflow-type separation case and can handle angles of attack, or sideslip, from approximately 30° to 90°.

Current separation prediction methods can be divided into two groups. The methods of the first group require the solution of the boundary-layer equations and are either of the differential or integral type. The methods of the second group predict separation based on simple formulas or empirical relations and are usually very fast and easy to apply. A summary and comparison of some of the methods in each group is contained in reference 10. One method from the latter group that lends itself particularly well to the present situation is the method of Stratford (ref. 11) which uses only the pressure distribution to predict boundary-layer separation. Although originally developed for two-dimensional flow over a flat plate, it has been shown by Spangler and Mendenhall in reference 12 to be effective for bodies in crossflow with only a slight modification. Although the work of references 11 and 12 considers both laminar and turbulent separation,

only the latter case is considered for the airship application.

The Stratford criterion is based upon the concept of dividing the boundary layer into inner and outer layers. By matching the two solutions at the juncture of the layers an equation is developed of the following form.

$$C_p\left(s\,\frac{dC_p}{ds}\right)^{1/2}(10^{-6}Re_s)^{-1/10} = F(s) \qquad (14)$$

where s is a streamwise distance parameter. The value of F(s) is found by experiment and, as noted by Stratford in reference 11, is independent of C_p.

The analysis that leads to equation (14) is based on the development of a boundary layer on a flat plate with a constant pressure imposed up to a distance s_m, followed by an adverse pressure gradient beyond s_m. For purposes of determining the parameter F(s), Stratford uses a virtual origin at a position s' such that an all-turbulent boundary layer starting at s' has the same thickness and velocity profile at s_m as the actual laminar-transitional-turbulent boundary layer starting at the plate leading edge (s=0). For the fully turbulent flow, reference 10 defines the location of the virtual origin (after dropping a very small term) as:

$$s_m - s' = \int_0^{s_m}\left(\frac{U_e}{U_m}\right)^4 ds \qquad (15)$$

For the present case of crossflow over a circular body, a favorable pressure gradient occurs from the stagnation point to the maximum velocity point on the flank. Application of equation (15) provides a virtual origin for the circular body case, with U_m the velocity at the flank of the body. For the circular body, a new pressure coefficient has to be defined based on the maximum velocity U_m.

$$C_p' = 1 - \left(\frac{U_e}{U_m}\right)^2 \qquad (16)$$

Using equations (14), (15), and (16), the separation point can be predicted as soon as an appropriate value for $F(s)$ at separation is selected. Based upon experimental evidence Stratford found separation to occur at the point where $F(s) = 0.4$. The results of reference 12 indicate good agreement with other separation prediction methods and data using this value.

For flow over inclined bodies of revolution at angles of attack less than 90°, the boundary layer has both an axial and a crossflow component. The longer run lengths tend to cause separation closer to the maximum velocity point on the flank of the body. As an approximate correction for angle of attack, the factor $F(s)$ was replaced with $F(s) \sin \alpha$ in the work of reference 12, with considerable success. That approach is used in the present analysis for angles of attack down to about 30°. Thus, the right hand side of equation (14) becomes $F(s) \sin \alpha$.

In modeling the hull of an airship, the surface is divided axially into a number of rings, each of which is divided circumferentially into a number of panels. The foregoing analysis for separation is applied to each ring along the length of the hull to locate (usually) two separation points.

Incorporation of this separation criterion into the potential flow model for the hull requires the computer to be able to make several nontrivial decisions. One such decision involves an airship hull in hover. Since there is no free stream, there is no well defined stagnation point in the normal sense. However, the pressure distribution calculated from purely potential flow considerations indicates the likelihood of flow separation in the vicinity of the rotors. But to apply the separation criterion the location of the stagnation point must be specified (i.e., the

stagnation point is the lower limit in the integral of equation (15)). Hence, when applying the separation criterion for a hull in the presence of rotors the point $s = 0$ (stagnation point) is defined as the location of maximum C_p. For the case of one rotor on a hull in hover, this point will be located on the side of the hull opposite to the rotor.

Since the inviscid pressure distributions which govern the onset of separation can be very steep for a powered hull in hover, a smoothing function is applied before taking the derivatives in equation (14). This is accomplished by fitting a cubic spline function to the pressure distribution and then using the coefficients of the cubic spline to calculate the derivatives.

Pressures in Separated Region

Because of asymmetries in the pressure distribution around the hull for all cases except the hull alone out of ground effect, the separation criterion is independently applied in both directions along each ring starting at the stagnation point. Thus two separation locations are determined independently of one another. The pressures at these two locations are then averaged to give the pressure in the separated region. The pressure on each panel in the separated region is then given this value. Thus the final pressure distribution is the inviscid pressure up to the separation points and the average inviscid pressure of the two separation points at all points downstream of separation in the wake.

CALCULATION PROCEDURE

For ease of computation all necessary computer programs for calculating loads on a complete HLA configuration have been combined into a single operational unit named HELIAIM (Heavy-Lifter Aerodynamic Interference Model). This includes a geometry program which calculates the locations of the corner points of the

hull source panels, the hull potential flow program, the rotor wake program, and the hull flow separation program. In this section the calculation sequence is outlined for a complete airship configuration with separation effects included.

The calculations proceed as shown on the following page. The first step is to determine the corner locations of the body source panels on the hull surface. A geometry program has been developed to generate these coordinates for a body of revolution consisting of a cylindrical center section of arbitrary length and ellipsoidal end sections. Unequal panel spacing both axially and circumferentially may be used if desired. These corner points are then used to establish the system of plane quadrilateral panels that represent the surface. The no-flow boundary condition is satisfied at one point on each panel - the control point. The panel centroid is taken as the control point. Thus, the next step is to determine the velocity induced at each of the control points by the rotor system.

For each rotor, its location, attitude, size, thrust coefficient, and angular rate are input, as indicated previously. The wake centerline of the rotor is located in the plane perpendicular to the rotor disk which contains the onset flow at the rotor center. This onset flow could be the free stream only or it could be the vector sum of the free stream and a hull-induced perturbation velocity. In the calculations made to date, only the free stream has been used. The skew angle is calculated to locate the wake centerline in this plane. Induced velocities at every hull control point are calculated from the rotor singularity model for each rotor present.

The rotor-induced velocities are then added to the free-stream velocity at each control point and the required source density distribution is determined. Once this is done the resultant flow velocities are calculated by adding the contributions

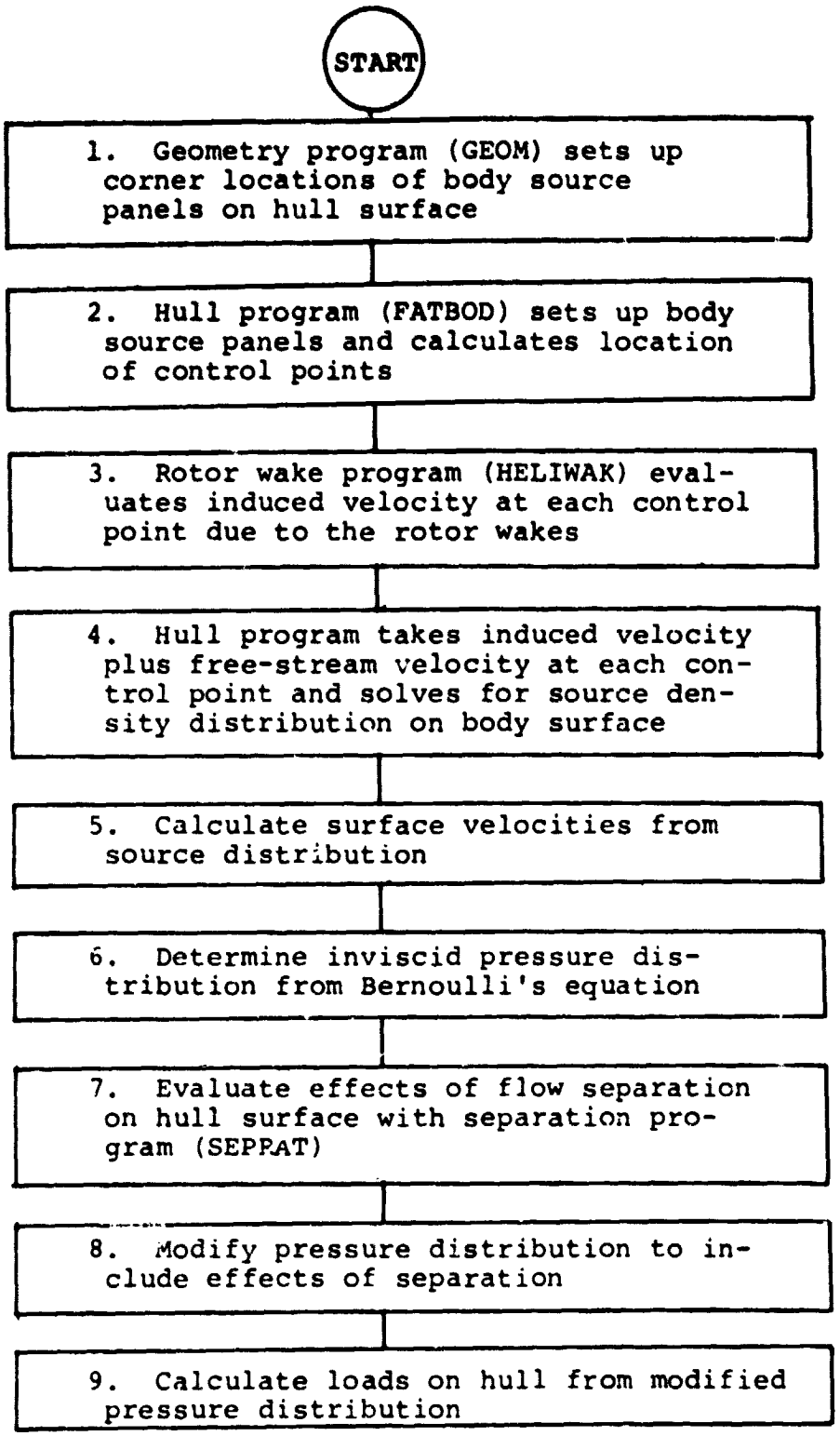

Sequence of Program Computations

of the source elements, the rotors, and the free-stream velocity. These velocities are next used to compute the inviscid pressure distribution over the hull surface from Bernoulli's equation.

The inviscid pressure distribution is next evaluated for possible flow separation according to the modified Stratford criterion described in the previous section. Separation effects are evaluated around the hull at each axial location, one ring at a time. If separation is found to occur, the pressure distribution downstream of separation is modified and the program moves on to the next ring. This complete modified pressure distribution is then used to calculate the total loads on the hull due to effects of free stream, rotor wakes, and flow separation.

At this point one could improve the calculations by iterating on the wake location that was determined only from the free-stream velocity. The hull program gives the value of the velocity at points away from the hull surface induced by the presence of the hull. Thus it would be possible to evaluate the velocity at the location of the rotors induced by the hull and other rotors, re-calculate the wake trajectories and the wake induced velocities on the hull surface, and repeat the set of computations until the loads converged to a final value. This procedure has not been incorporated in the program at this time.

The presence of a ground plane can be incorporated by making use of symmetry provisions in the Douglas program. The only difficulty lies in handling the rotor wake-induced velocities properly. In the ground plane case, an image rotor exists for each real rotor. The program accounts properly for the image hull source contribution to the velocities at a control point, so an additional feature is used to add on image rotor induced velocity as well. Otherwise, the calculation proceeds as before.

RESULTS

In this section, a number of results are shown to indicate the capabilities of the method and the types of loading that can be induced by rotors and rotor wakes adjacent to an airship hull. For purposes of illustration, the analytical methods are applied to the "Heavy Lift Airship" (HLA) configuration that evolved from the NASA sponsored study reported in reference 1. An additional reason for using this configuration is that some small scale model data on loads are available from reference 3.

A drawing of the HLA configuration is shown in figure 4. The dimensions indicated are full scale. The hull is circular in cross section and has a cylindrical center section and ellipsoidal ends. The four rotors are mounted relatively low on the cylindrical portion of the hull. The positive x-direction is towards the bow, although the configuration is symmetric fore and aft.

The predicted results obtained on this configuration are compared with the data of reference 3 wherever possible. These are the only data of this kind available, to our knowledge. As a general comment on these comparisons, it is noted that considerable difficulty was experienced with the instrumentation in the wind tunnel tests. One overall and four rotor six-component balances were used in the tests, generally measuring loads of a few pounds or less. The hull loads were obtained as the difference between the total load and the sum of the four rotor loads. A good bit of data was lost or suspect because of balance failure, vibration, and amplifier drift at the low signal levels. As a result the accuracy of the data is somewhat questionable, although the general levels and trends ought to be good.

Hull Alone

For purposes of modeling the hull, its surface was divided into panels, with 16 unequally spaced along the length and 24 equally spaced around the circumference. The panel arrangement is shown in figure 5. This arrangement is a compromise between a large number of panels to get detailed pressure distributions, particularly near separation, and a small number of panels to minimize computation times. From an accuracy standpoint, one could use fewer panels, particularly on the cylindrical section. This is shown in figure 6, which compares pressure distributions for the 16 × 24 arrangement with those for a 6 × 8 arrangement for the hull in crossflow. The two agree well except on the ellipsoidal nose.

For the hull alone out of ground effect, a potential flow solution would indicate no net force for all combinations of angles of attack and sideslip. Thus all loads are due to the influence of flow separation on the hull. Figure 7 shows the predicted separation lines on the hull for zero angle of attack and various sideslip angles. At $\beta = 90°$, the separation line is about 130° from the windward meridian except near the very ends of the hull and is symmetric fore and aft. At smaller sideslip angles, the separation line shifts such that the nose remains unseparated and more of the aft end is in separated flow.

Measured and predicted side force and yawing moment variation with sideslip angle for the hull out of ground effect are shown in figure 8. The data are from reference 3 and are based on a roughened hull which was found necessary to ensure turbulent separation. The predicted side force is lower than the measured results except at $\beta = 90$ but shows the same trend as the data. The predicted yawing moment also shows the same trend as the data but is somewhat low in the 30° to 60° range.

The influence of ground effect is shown in the next two figures. Figure 9 shows circumferential pressure distributions near the center of the hull for the 90° sideslip case with and without ground effect. Over the top of the hull, the pressures are very similar, and separation occurs about a degree further around the hull. Over the lower surface, the ground effect causes a higher velocity and a more negative peak pressure coefficient. The increased adverse pressure gradient causes separation to occur 2° to 3° earlier. The average of the two (top and bottom) pressures at separation in ground effect is a somewhat lower pressure coefficient than for the out-of-ground effect case.

Figure 10 shows the side-force coefficient variation with sideslip at H/D=1. In this case the trend and the predicted values are in reasonable agreement with the data. Because of the lower separation pressure the predicted side force increases a small amount due to ground effect (compare figures 8 and 10). The data indicate that the influence of the ground on side force is small but no trend is evident.

Rotor Alone

To validate the accuracy of the rotor wake program some calculations were made for a single rotor operating in a uniform flow and compared with experimental results. This section discusses these comparisons. Although a great deal of research, both theoretical and experimental, has gone into the accurate representation of the rotor wake, the purpose of most of this research has been the accurate prediction of induced inflow at the rotor disk. The result of this is that existing induced velocity data is in the vicinity of the rotor disk and the wake and not in the relatively distant field where the HLA hull would be located. Thus, the comparisons in this section are not at locations representative of the HLA hull. The assumption is made, therefore, that

accurate representation of the rotor wake near field implies accurate representation of the far field.

The rotor wake analysis assumes that the wake skew angle is known a priori. As described in Appendix A the skew angle is evaluated from momentum theory for the particular combination of rotor geometry, rotational speed, loading, and forward velocity. The value derived from momentum theory is compared to experimental results taken from reference 13 in figure 11. The agreement is quite good, with skew angle being predicted within a few degrees by momentum theory. As a point of reference, in the HLA configuration results to be discussed subsequently, for a typical disk loading of $478 N/m^2$ ($9 lbs/ft^2$) in a free-stream velocity of 15.4m/sec (30 knots) the skew angle is approximately 56°.

For a given rotor, the total induced velocity at any point is the sum of the contributions from the four individual vortex systems. Figure 12(a) shows these relative contributions at a point outboard and just above the rotor disk (the nearest hull control point of the HLA configuration). Note that the four component velocities in figures 12 are not additive to get the total because they are magnitudes of vectors which have different directions. As can be seen, the major contribution is from the vortex rings. The difference between the total induced velocity and the induced velocity due to the vortex rings is generally within five percent of the free-stream velocity for all velocities of interest.

This difference is even less at points further away from the rotor disk. The total induced velocity and that induced by the vortex rings at a point near the nose of the HLA configuration are compared in figure 12(b). Here the difference is essentially negligible, indicating that for points in the far field of the rotor wake the wake-induced velocity can be adequately represented by accounting for only the ring vorticity (i.e., using an actuator disk model for the rotor wake).

Comparisons of induced velocity are made in figure 13 with experimental results from reference 14 for a rotor alone in a free stream flow. These curves show the variation in the component of induced velocity normal to the rotor disk, normalized by the induced velocity derived from momentum theory, across the plane of the rotor disk at two streamwise positions and two heights above the disk. Agreement is good at most locations across the disk, although the predicted results tend to show more right-to-left asymmetry due to advancing/retreating blade aerodynamics than do the data. The free-stream velocity for the particular set of conditions analyzed in figure 13 is 6.02 times the jet velocity.

Since these experimental results show only the normal component of induced velocity, some calculations were made of induced velocities at a number of points in proximity to the rotor wake to determine the general nature of the induced flow. Figures 14(a) and 14(b) show the results at points one-half rotor radius away from the rotor wake and at 90° intervals about the wake starting at the x-axis. The velocity vectors shown are scaled relative to the free-stream velocity. The thrust and flow conditions used are typical of the rotor used in the HLA configuration.

In figure 14(a), the side view shows the rotor-induced velocities directed roughly normal to the wake axis, except in the vicinity of the rotor disk. Upstream and downstream of the wake, the induced velocities are directed upstream, whereas outboard of the flanks of the wake cylinders, the induced velocities are directed downstream. This pattern generally resembles that induced by a doublet which is used in two dimensional potential flow to represent the induced velocity of a solid cylinder in a uniform flow, as shown in the sketch.

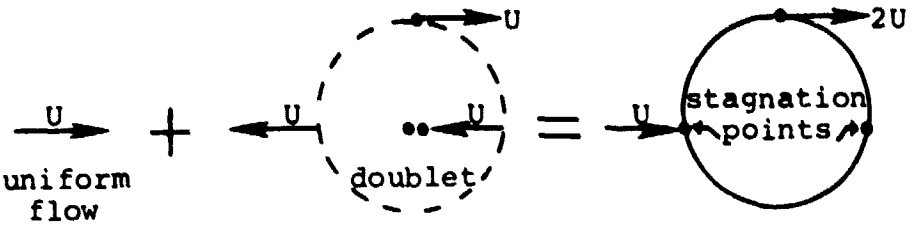

Thus, the singularity representation of the wake tends to make the wake resemble a solid cylinder around which the free stream passes.

The flow near the rotor disk is generally into the disk, as would be expected. Essentially, the rotor disk acts as a sink to attract the flow from all directions.

Figures 14(a) and 14(b) together indicate that the induced velocity is higher on the positive y_R side of the disk, which is the advancing blade side.

These induced velocity characteristics are useful in analyzing the aerodynamic interference effects induced on the hull by adjacent rotors which are discussed in the following section.

Hull-Rotor Combinations

Results for five cases are presented to indicate the nature of the predicted interference effects between the rotors and hull for the HLA configuration. The five cases consist of a hover case out of ground effect, an axial free-stream flow in and out of ground effect, and a crossflow case in and out of ground effect.

The first case is the HLA configuration in zero free stream flow with a single rotor on the forward left side developing thrust with a disk loading of 395 N/m^2 (8.26 psf). This case corresponds to a test condition run in the wind tunnel program and also illustrates well the interference effects of a single rotor. Since there is no free-stream flow, all hull loads are induced by the rotor.

The velocities induced by the rotor at the panel control points on the hull at an axial station 3m (9 feet) aft of the rotor-center axial station are shown in figure 15. The vector scale length is shown relative to the velocity V_j in the rotor plane. As would be expected, the rotor disk and wake act as a sink and induce flow towards the rotor. Over most of the hull, the induced velocity is less than 0.1 V_j, but adjacent to the rotor, the highest induced velocity is about 0.3 V_j.

Predicted circumferential pressure distributions at three axial stations are shown in figure 16. The pressure coefficient is nondimensionalized by a dynamic pressure corresponding to a unit velocity. The station that corresponds to the induced velocities is shown by the circles. Over the top of the hull where the velocities are small ($45° < \theta < 270°$), the pressure coefficients are small. As one approaches the high velocity region opposite the rotor ($\theta = 330°$), the pressure coefficients reach very large negative values ($\theta = 310°$ and $350°$). Since the induced flow along the hull is towards the $\theta = 330°$ point on both the lower and left portions of the hull, a "stagnation point" should occur where these flows meet, which is shown by the rise in pressure coefficient to about -40 at $\theta = 330°$. Directly opposite the rotor center, the pressure coefficient should rise to zero, but at the 15 meter station, there is an axial component of the flow which prevents this value being reached.

At $x = 32$ meters, which is near the forward edge of the rotor, the pressure coefficients show an acceleration of the flow near the rotor ($\theta = 320°$), but not the "stagnation point" behavior of the 15 meter station. The flow is more affected by the axial component in this case. At $x = -5$ meters, which is well aft of the rotor, the flow is again principally forward axially along the hull, and the pressure coefficients are small.

No flow separation calculations were made for this case. It is possible with the adverse pressure gradients that exist from

310° to 320° and 350° to 340° at the 15 meter station that separation would occur over perhaps a 20° band; this would be characteristic of axial stations near the rotor center (x = 17m). The pressure recovery to $C_p \tilde{=} -40$ at $\theta = 330°$ would be reduced somewhat, if separation does occur.

The integrated hull loads for this case and the corresponding experimental values from reference 3 are shown below.

Quantity	Predicted	Measured
C_Y	-.053	+.472
C_z	+.029	-.002
C_m	-.011	not reported
C_n	-.022	not reported

The predicted values are all consistent with a low pressure region on the lower, left, forward part of the hull (adjacent to the rotor); that is, a downward normal-force, a left side-force, a nose-down pitching-moment and a nose-left yawing-moment. The data show signs for the C_Y and C_z opposite those of the predicted values. No moment data are available for a consistency check. The reason for the differences is not known. The hull-alone data are obtained by differencing the total load from the main balance and the sum of the four rotor balance loads, and in most cases the difference is small compared to the two numbers being differenced. Also the hull-alone data include the effect of the rotor support arms, and the size of this effect is difficult to assess. These may be contributing factors to the differences.

The second and third cases are a hull with four rotors in an axial flow ($\alpha = \beta = 0$) of 15.4m/s (30 knots). In the second case, the vehicle is out of ground effect and in the third case, the hull centerline is one hull diameter above the ground. Out of ground effect, the forward rotors (Nos 1 and 4) have a disk

loading of 609 N/m^2 (12.73 psf) and the aft rotors 521 N/m^2 (10.88 psf), which are the values measured in the wind tunnel for this case. The resulting wake skew angles are 51° and 54°, respectively.

In ground effect, the disk loading of all four rotors is 479 N/m^2 (10 psf), again in consonance with the tunnel tests, and the skew angle is 56°.

The wake configurations are shown in figure 17 for wake skew angles of 56°. In the second case (without ground effect), there is no image system and the rotor wakes are swept slightly forward of those shown in the figure. In the third case, the image system exists, as shown. The sketch shows a limitation in the use of the Heyson rotor model, which because of the analytical integrations performed, is constrained to a straight centerline. The image wakes from the forward rotors come close to the aft end of the hull and tend to cause unrealistic induced loads. A more realistic wake model would be curved to approach and become parallel to the ground. To go to a curved wake would require dropping the analytical integration and modeling the wake with a series of vortex rings and axial finite-length vortex filaments, with numerical summation of the induced velocities, as was done in reference 15.

Rotor-induced velocities in and out of ground effect are shown in figure 18 for an axial station near the center of the hull between the fore and aft set of rotors. There is some influence of the image system on the velocities, but the two sets are generally similar. The rotors induce a downwash over the top of the hull, an upwash over the bottom of the hull, and outward flow towards the rotor wakes near the rotor disks. The flow is not symmetrical right-to-left because the rotors are all rotating in the same direction and their induced velocities in a crossflow are different on the advancing and retreating sides.

The corresponding circumferential pressure distributions are shown in figure 19. Over the top of the hull, ($0° < \theta < 180°$),

the pressure is relatively uniform and not greatly different from the hull-alone value. There are small pressure coefficient peaks (least negative) at $\theta = 210°$ and $330°$ which correspond to the crossflow velocity reversal along the hull opposite the rotors. Over the bottom portion of the hull there is a suction peak induced by the high rotor-induced velocities.

The integrated hull loads for these cases and the measured values from reference 3 are shown below. No predicted flow separation effects are included in these calculations.

	Predicted Values		Measured Values	
Quantity	Out of G.E.	In G.E.	Out of G.E.	In G.E.
C_Y	-.006	+.088	not reported	not reported
C_z	+.156	+.272	-.443	-.035
C_m	-.024	+.068	not reported	not reported
C_n	-.135	-.097	not reported	not reported

Out of ground effect, the predicted centers of pressure for both the vertical and lateral forces are forward of the hull center, as was the case for the single rotor-hull in hover. In the presence of the ground, the side force changes sign and its center of pressure moves aft of the hull center, since the sign of the yawing moment is not changed. The vertical force maintains the same sign, increases in magnitude and its center of pressure moves aft of the hull center, since the sign of the pitching moment changes. The aftward shift of the centers of pressure is probably due to the influence of the image wake on the flow over the aft end of the hull.

Only the normal-force results are available from the tests. Although the change in force due to the ground presence has the same sign as the prediction, the data indicate an opposite sign to the predicted values. Again the reasons for the differences are not known.

The fourth and fifth cases are a hull with four rotors in a crossflow ($\alpha = 0$, $\beta = -90°$) of 15.4 m/s (30 knots). The fourth case is for the vehicle out of ground effect and the fifth is for the hull centerline one diameter above the ground. All four rotors have a disk loading of 478 N/m^2 (10 psf) out of ground effect and in ground effect; the wake skew angles are 56°.

The wake configuration is shown in figure 20. In this case, the image wakes do not intersect the hull, but they come fairly close and do induce some large velocities on the downstream surface of the hull. As indicated previously, a curved wake would provide a more accurate simulation.

Rotor induced velocities at an axial station near the aft rotor center are shown in figure 21. Without ground effect, the rotors induce a downward flow over the hull which is largest near the two rotor disks. In the presence of the ground plane, the image wake induces some large velocities directed away from the wake generally towards the free stream flow. Thus, large differences in induced velocities occur due to the ground plane effect.

The resulting pressure distributions are shown in figure 22. There are three curves shown: a hull alone out of ground effect (without separation) and the hull with rotors in and out of ground effect (with separation). Over the top of the hull ($0 < \theta < 120°$), the three curves are similar. Separation is predicted to occur at about 130° for both in and out of ground effect. The pressure distribution over the lower side of the hull up to separation is considerably different than the hull alone. The influence of the rotors is to induce a flow counter to the free stream flow over the lower part of the hull, which yields a higher pressure than for the hull alone. Separation occurs on the lower part of the hull about 130° around from the windward meridian for both the in and out of ground effect cases.

It is of interest to note in connection with figures 21 and 22 that while the rotor-induced velocities show the reversal in direction along the hull that was noted in connection with the hover case (figures 15 and 16), when the free stream is added, the reversal in total velocity along the surface does not occur. That is, the pressure distribution with a free stream (figure 22) does not show the "stagnation point" behavior that the hover case shows (figure 16). As the disk loading increases and/or the free stream decreases, the pressure distribution would proceed from the more regular type of figure 22 to the more complicated one of figure 16, with or without ground effect.

The predicted and measured loads on the hull for these conditions are shown in the table below. A large side (or drag) force

Quantity	Predicted Values		Measured Values	
	Out of G.E.	In G.E.	Out of G.E.	In G.E.*
C_Y	1.59	.74	2.22	2.77
C_z	-.18	-.26	1.09	1.54
C_m	-.067	-.083	not reported	not reported
C_n	.05	+.57	not reported	not reported

is predicted due to separation out of ground effect which is decreased in the presence of the ground. This effect is due to the proximity of the image wake and would probably be much less significant with a curved wake model. The measured side force out of ground effect is somewhat higher than the predicted value. Since the disk loading changed somewhat for the tests in ground effect, the force changes due to presence of the ground are not comparable to the predicted changes. The predicted normal forces are small and upward in direction, because of the absence of the suction peak on the lower hull surface. Again there is a difference in sign between predicted and measured normal force, which cannot be explained.

*These data correspond to a disk loading of 539 N/m^2 (11.25 psf).

Systematic Rotor Effects

One purpose of developing this analytical method to predict the effects of aerodynamic interference on airship configurations is to use the method to investigate various design changes, such as hull shape or rotor placement. By studying the results of such changes not only can an optimum design with least unfavorable interference be determined but much can also be learned about the basic interaction mechanisms and how they affect the total vehicle.

A few results on the effects of rotor placement are presented in this section. The baseline HLA hull (figure 4) was used throughout and only the vertical and lateral locations of the rotors were changed. The axial locations remain the same as in figure 4. These results are for a vehicle out of ground effect in a crossflow ($\alpha = 0°$, $\beta = -90°$) of 9.14 m/sec (30 ft/sec), with a disk loading of 478 N/m^2 (10 psf), and with separation on the hull.

The effect on hull loads of vertical placement of the rotors is shown in figure 23. The horizontal distance between the tip of the rotor and the surface of the hull has been kept constant at the same value as the baseline configuration in figure 4. Side force and yawing and pitching moments are only slightly affected by rotor vertical placement. The normal force, however, is strongly affected, changing from an upward force (negative C_z) for high rotor positions to a downward force when the rotor is even with the bottom of the hull ($Z_Q/R = 1$). Examination of the induced velocity fields revealed that when $Z_Q/R = 1$ the rotor-induced velocity over the hull was directed downwards everywhere and was very large in magnitude. Conversely, when $Z_Q/R = 0$ there was a region of upwash on the lower part of the hull and the magnitude of the downwash was much less. Hence, the vertical rotor vertical placement has a substantial effect on the rotor-induced velocity on the hull and, subsequently, on the hull vertical loads. For this example, a change in C_z from -0.6 to 0.4 with rotor height change corresponds to a change in hull vertical force approximately equal to the thrust of one rotor.

Effects due to changes in lateral spacing are shown in figure 24. In this study the vertical location of the rotors is $Z_Q/R = 0.5$. Normal force, yawing moment, and pitching moment all decrease as the rotors are moved farther away, while the side force overshoots and then decreases towards the hull-alone value. Thus, the hull loads are also strongly affected by the lateral location of the rotors.

The results in this section, although limited, indicate the importance of systematic studies of rotor locations, under many different flow conditions, to properly locate the rotors relative to the hull to either minimize adverse rotor interference or obtain a favorable influence.

CONCLUDING REMARKS

An analytical method has been developed to predict the perturbation pressure distribution induced on an airship hull by adjacent rotors. The method accounts for flow separation on the hull at angles of attack and sideslip above about 30°, where there can be considerable interaction between the rotor induced perturbation effects and the separation-induced hull loads. A number of cases were calculated and are reported herein to illustrate the nature of the hull-rotor interaction. This section contains some comments on the work and results.

One important limitation of the method is the constraint imposed by the Heyson analytic wake model of a straight, semi-infinite wake. Out of ground effect, the limitation is probably of little importance. The significant wake-induced effects are caused by that portion of the wake in close proximity to the hull. It is relatively simple to modify the wake skew angle to best locate the wake relative to the hull considering both the free stream and the hull flow perturbation. This approach should suffice for all configurations except those in which the rotors are very close

to and high on the hull and have wakes with many diameters of length close to the hull. However, in ground effect, it is felt that a straight wake is inadequate, and a curved wake model is necessary. In this case, one must forego the analytic model and use a numberical model such as that of reference 15. This numerical model uses vortex rings concentric with a centerline which may be curved arbitrarily. Since the results of figure 12 show the vortex rings of the Heyson model to be the major contributor to rotor-induced velocities on the hull, the numerical model should be satisfactory. The vortex ring model has the additional feature of modeling entrainment through change in the diameters of the rings along the wake, should that be desirable. For high crossflow, a surface vortex quadralateral distribution can be added to model blockage, which will show much the same characteristics as in figure 14. This model has been implemented in other work at Nielsen Engineering and can be readily incorporated in the airship-rotor interaction model.

Little was said of the influence of the hull on the rotor performance. In the cases examined, the experimental thrust coefficients from reference 3 were used. These tests showed only a small influence of hull presence on rotor thrust (generally less than 10 percent), even for the case of a rotor operating downstream of the hull in crossflow. There was a greater influence of ground presence on rotor thrust (as high as 20 percent). Some effort needs to be made to estimate these effects and develop a systematic approach to calculate the change in rotor thrust as the rotor is brought into proximity with the hull, in and out of ground effect.

Due to limitations in scope of the effort, no calculations were made to illustrate the capability of the method to model a hull with tail surfaces to examine the influence of tails on hull-rotor interference. The Douglas program has been used by NEAR to make calculations for deltoid airship configurations with tails,

although no rotor-induced effects were included. The method would be limited to angles of attack and sideslip for which no separation occurs on the tails, although one would probably not operate an airship with tails at very large angles, at least in steady state.

The approach that was used to calculate the pressures on the hull in large regions of separated flow is rather straightforward. The approach works well for the hull alone over a large angle range and is felt to be a good initial approach to model this phenomena, which can be important in many cases. The method becomes less satisfactory when the two pressures at separation on a given ring begin to differ substantially due to rotor-induced effects, since these two pressures are averaged. In order to get a better understanding of this problem and develop a more accurate model, it is essential to perform experiments in which pressure distributions are measured on a hull with rotor interaction over a range of disk loadings, free stream velocities, and angles of sideslip.

The discrepancies in sign between predicted and measured normal force need to be resolved. One of the questions that arose in the work was whether or not the hull source singularity model was providing a zero net source strength in cases of nonuniform onset flow. For the hull-alone out of ground effect, one sees a symmetry fore-and-aft or circumferentially, depending on the direction of the onset flow, which provides zero net source strength. Since the Douglas program does not require zero net strength as a condition on calculation of source strengths, the computer program was modified to sum the source strengths after they are calculated to investigate this question. Results show that with a nonuniform onset flow, the surface source strengths are redistributed nonuniformly to cancel locally high onset flow velocities in such a way that the zero net source strength condition is preserved over the entire body, provided it is closed. Since no other

fundamental issues arise in application of the methods to this problem, the differences in predicted and measured normal force are attributable either to the separation and wake pressure aspects of the calculation or to problems with the small scale data. Only carefully executed experiments to obtain surface pressure distributions and surface flow visualization will resolve this problem.

Finally, the Douglas program is not well suited in its original form to the hull-rotor problem because its emphasis is on single body problems (as opposed to ground-plane image cases) with predominately lifting-surface configurations. Program modifications have been made to handle every rotor-airship case of interest, but many cases are inefficient to run and it is very difficult to prepare input. Additional work needs to be done to simplify the program and make it much easier to prepare input and interpret the output.

In summary, the recommendations for additional investigations include the following:

- experiments at high Reynolds numbers on typical hull-rotor configurations in which simultaneous measurements of rotor and hull loads, surface pressures, and surface flow visualization are taken
- implementation of a curved wake rotor model to improve the prediction method for cases in ground effect and with closely coupled rotors. A part of this task is the definition of the wake centerline location for flow conditions of interest
- development of methods for estimating the influence of the hull on thrust of rotors adjacent to the hull
- improvement in the separation location and wake pressure models to include nonuniformities in the wake flow region, based on critical experimental results

- modification of the computer program to make its operation more efficient and to make it user oriented in terms of input preparation and output interpretation.

Nielsen Engineering and Research, Inc.
Mountain View, California
April 1978

APPENDIX A

DERIVATION OF ROTOR WAKE MODEL

As discussed in the main report, the mathematical model used to describe the rotor wake is based on the classical vortex theory of a non-contracting wake. The model, shown in figure 2 of the main report, divides the wake into four vortex systems. The origin of each of these vortex systems has been described in the main report and will not be repeated here. In this section the induced velocity at a point due to each of these vortex systems is derived. The coordinate system used in this development is given in figure A.1. The onset velocity, by definition, lies in the X_R, Z_R plane.

FORM OF BLADE CIRCULATION

As explained in the main report, the blade circulation varies in the azimuthal plane according to the relation

$$\Gamma = \Gamma_0 + \Gamma_1 \sin \psi \tag{A1}$$

Now, the incremental thrust along the blade is

$$dT = \rho_\infty U_T \Gamma \, dr \tag{A2}$$

where U_T is the tangential component of the resultant velocity at the blade element, i.e.

$$U_T = \Omega r + \mu \Omega R \sin \psi \tag{A3}$$

Therefore, the rotor thrust is given by

$$T = \frac{b}{2\pi} \int_0^{2\pi} \int_0^R \rho_\infty (\Omega r + \mu \Omega R \sin \psi)(\Gamma_0 + \Gamma_1 \sin \psi) dr d\psi \tag{A4}$$

$$T = b\rho_\infty \frac{\Omega R^2}{2} (\Gamma_0 + \mu\Gamma_1) \tag{A5}$$

Expressed in terms of the non-dimensional thrust coefficient equation (A5) becomes

$$C_T \equiv \frac{T}{\rho\pi R^2 (\Omega R)^2} = \frac{b}{2} \frac{\Gamma_0 + \mu\Gamma_1}{\Omega\pi R^2} \tag{A6}$$

Defining the thrust moment as

$$M_T \equiv \int_0^R \rho_\infty (\Omega r + \mu\Omega R \sin\psi)(\Gamma_0 + \Gamma_1 \sin\psi) r \, dr, \tag{A7}$$

and carrying out the integration gives

$$M_T = \rho_\infty \Omega R^3 \left[\frac{\Gamma_0}{3} + \left(\frac{\Gamma_1}{3} + \frac{\mu\Gamma_0}{2} \right) \sin\psi + \frac{\mu\Gamma_1}{2} \sin^2\psi \right] \tag{A8}$$

If the assumption is made that flapping terms above the first harmonic are negligible, then the thrust moment can be shown (reference A.1) to be independent of the azimuth angle ψ. Thus, from equation (A8),

$$\frac{\Gamma_1}{3} + \frac{\mu\Gamma_0}{2} = 0 \tag{A9}$$

or

$$\Gamma_1 = \frac{-3}{2} \mu\Gamma_0 \tag{A10}$$

Substituting this expression into equation (A6) the following relations for blade circulation in terms of thrust coefficient are obtained.

$$\Gamma_0 = \frac{2C_T \Omega\pi R^2}{b\left(1 - \frac{3}{2}\mu^2\right)} \tag{A11}$$

$$\Gamma_1 = \frac{-3\mu C_T \Omega \pi R^2}{b\left(1 - \frac{3}{2}\mu^2\right)} \tag{A12}$$

EVALUATION OF WAKE SKEW ANGLE

The wake skew angle is defined as

$$\chi = \tan^{-1} \frac{-\mu}{\lambda} \tag{A13}$$

where

$$\lambda = \frac{V_\infty \sin \alpha + V_j}{\Omega R}$$
$$\mu = \frac{V_\infty \cos \alpha}{\Omega R} \tag{A14}$$

Hence, the normal component of the induced velocity at the rotor center, V_j, is required to determine the skew angle. Using classical momentum theory to calculate V_j (e.g. reference A.1) the following relation is obtained

$$V_j = \frac{-1/2\ C_T\ \Omega R}{\sqrt{\mu^2 + \lambda^2}} \tag{A15}$$

Substituting the values for μ and λ, the value of V_j is given by

$$V_j^4 + (2V_\infty \sin \alpha)\ V_j^3 + (V_\infty^2)\ V_j^2 + \left[-C_T^2\ \frac{(\Omega R)^4}{4}\right] = 0 \tag{A16}$$

Equations (A13), (A14), and (A16) are thus combined to yield a value for the wake skew angle.

VORTEX INTEGRAL RELATIONS

Central or Root Vortex

This vortex lies along the wake axis and is the superposition of the root vortices of all blades. Hence, its circulation strength is the sum of the blade bound vortex strengths, i.e.,

$$\Gamma_R = b\Gamma_o \tag{A17}$$

To determine the induced velocity of this single vortex filament the following form of the Biot-Savart Law is used.

$$\vec{V}_R(\vec{r}) = \frac{-\Gamma_R}{4\pi} \int \frac{\vec{ds} \times (\vec{r}-\vec{s})}{|\vec{r}-\vec{s}|^3} \tag{A18}$$

From figure A.2 the following quantities are determined by inspection.

$$\vec{s} = (L \sin \chi \, \vec{i} - L \cos \chi \, \vec{k}) \tag{A19}$$

$$\vec{ds} = (\sin \chi \, \vec{i} - \cos \chi \, \vec{k}) dL \tag{A20}$$

$$\vec{r}-\vec{s} = (x_R - L \sin \chi)\vec{i} + y_R \vec{j} + (z_R - L \cos \chi)\vec{k} \tag{A21}$$

Substituting equations (A19), (A20), and (A21) into equation (A18) gives the following three integral equations for the three components of velocity induced by the root vortex.

$$U_R = \frac{-b\Gamma_o}{4\pi} \int_o^\infty \frac{y_R \cos \chi \, dL}{[(x_R - L \sin \chi)^2 + y_R^2 + (z_R - L \cos \chi)^2]^{3/2}} \tag{A22}$$

$$V_R = \frac{b\Gamma_o}{4\pi} \int_o^\infty \frac{\sin \chi (z_R - L \cos \chi) + \cos \chi (x_R - L \sin \chi)}{[(x_R - L \sin \chi)^2 + y_R^2 + (z_R - L \cos \chi)^2]^{3/2}} \, dL \tag{A23}$$

$$W_R = \frac{-b\Gamma_o}{4\pi} \int_o^\infty \frac{y_R \sin \chi \, dL}{[(x_R - L \sin \chi)^2 + y_R^2 + (z_R - L \cos \chi)^2]^{3/2}} \tag{A24}$$

Outer Wake

Since the outer wake is composed of both circumferential and axial vorticity, the combined strength being the strength of the tip vortex, the relation between these two systems must first be determined. This is done in the following manner.

Assume that one vortex element is formed per revolution per blade. Then the number of elements formed per unit time is $b\Omega/2\pi$. These elements are carried off with the velocity

$$\Omega R \sqrt{\mu^2 + \lambda^2} \tag{A25}$$

the wake velocity at the rotor. Therefore, the vorticity on the edge of the wake is

$$\frac{\Gamma b\Omega/2\pi}{\Omega R \sqrt{\mu^2 + \lambda^2}} = \frac{d\Gamma}{dL} = \frac{d\Gamma_o}{dL} + \frac{d\Gamma_1}{dL} \sin \psi \tag{A26}$$

In one revolution the circumferential distance traveled by a blade tip is $2\pi R$ and the axial distance traveled is L. The relation between the axial and the circumferential vorticity is best seen by unrolling one revolution worth of vorticity shed by one blade as in the following sketch

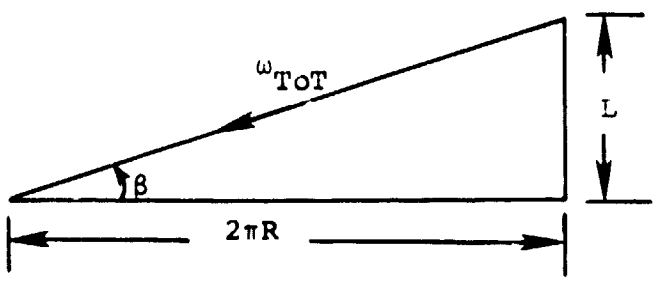

The axial vorticity is $\omega_a = \omega_{ToT} \sin \beta$, and the circumferential vorticity is $\omega_c = \omega_{ToT} \cos \beta$. Hence, the total vorticity is

$$|\vec{\omega}_{ToT}| = \sqrt{\omega_a^2 + \omega_c^2} = \omega_{ToT} \tag{A27}$$

Vectorially, this is written $\vec{\omega}_a + \vec{\omega}_c = \vec{\omega}_{ToT}$. Since one revolution occurs in $2\pi/\Omega$ sec., then using the wake velocity at the rotor given by equation (A25) the distance L becomes

$$L = 2\pi R \sqrt{\mu^2 + \lambda^2} \tag{A28}$$

If $L = 0$ $(\Omega \to \infty)$ then all the vorticity is circumferential and if $L \to \infty$ $(\Omega \to \infty)$ then all the vorticity is axial. Thus the assumption is made that the ratio of axial vorticity to circumferential vorticity is in the same ratio as $L/2\pi R$, i.e.,

$$\frac{\omega_a}{\omega_c} = \frac{L}{2\pi R} = \sqrt{\mu^2 + \lambda^2} \tag{A29}$$

or

$$\omega_a = \omega_c \sqrt{\mu^2 + \lambda^2} \tag{A30}$$

Substituting equation (A30) into equation (A27).

$$\omega_c = \frac{\omega_{ToT}}{[1 + \mu^2 + \lambda^2]^{1/2}} \tag{A31}$$

Using the expression for the total vorticity given by equation (A26), the circumferential vorticity is written in the following form.

$$\left(\frac{d\Gamma_c}{dL}\right) = \frac{b\Omega}{2\pi} \frac{1}{\Omega R \sqrt{\mu^2 + \lambda^2}} \frac{1}{[1 + \mu^2 + \lambda^2]^{1/2}} (\Gamma_0 + \Gamma_1 \sin \psi) \tag{A32}$$

The relation for the axial vorticity is found by combining equations (A30) and (A32).

$$\left(\frac{d\Gamma_a}{dR\psi}\right) = \frac{b\Omega}{2\pi} \frac{(\Gamma_o + \Gamma_1 \sin\psi)}{\Omega R[1 + \mu^2 + \lambda^2]^{1/2}} = \mu^2 + \lambda^2 \left(\frac{d\Gamma_c}{dL}\right) \qquad \text{(A33)}$$

Having found expressions for the axial and circumferential vorticity, the analysis can proceed to the determination of the induced velocities due to these two vortex systems. The induced velocity due to the circumferential vorticity will be treated first.

Circumferential vorticity.- From the Biot-Savart Law, the induced velocity can be written as

$$d\vec{V} = \frac{-1}{4\pi}\left(\frac{d\Gamma_c}{dL}\right) \frac{d\vec{s} \times (\vec{r}-\vec{s})}{|\vec{r}-\vec{s}|^3} dL \qquad \text{(A34)}$$

From figure A.3, the following relations can be obtained.

$$s = \vec{i}(R\cos\psi + L\sin\chi) + \vec{j}(R\sin\psi) + \vec{k}(-L\cos\chi) \qquad \text{(A35)}$$

$$d\vec{s} = [\vec{i}(-R\sin\psi) + \vec{j}(R\cos\psi)]d\psi \qquad \text{(A36)}$$

$$\vec{r}-\vec{s} = \vec{i}(x_R - R\cos\psi - L\sin\chi) + \vec{j}(y_R - R\sin\psi) + \vec{k}(z_R + L\cos\chi) \qquad \text{(A37)}$$

Substituting the above expressions into equation (A34), the following relations are obtained for the velocities induced by the circumferential vorticity.

$$U_c = \frac{-R}{4\pi}\int_0^{2\pi}\int_0^{\infty}\left(\frac{d\Gamma_c}{dL}\right)\frac{(z_R+L\cos\chi)\cos\psi\, dL d\psi}{[(x_R-R\cos\psi-L\sin\chi)^2+(y_R-R\sin\psi)^2+(z_R+L\cos\chi)^2]^{3/2}} \qquad \text{(A38)}$$

$$V_c = \frac{-R}{4\pi} \int_0^{2\pi} \int_0^{\infty} \left(\frac{d\Gamma_c}{dL}\right) \frac{(z_R+L\cos\chi)\sin\psi \; dL d\psi}{[(x_R-R\cos\psi-L\sin\chi)^2+(y_R-R\sin\psi)^2+(z_R+L\cos\chi)^2]^{3/2}} \tag{A39}$$

$$W_c = \frac{-R}{4\pi} \int_0^{2\pi} \int_0^{\infty} \left(\frac{d\Gamma_c}{dL}\right) \frac{(x_R\cos\psi-y_R\sin\psi+R+L\sin\chi\cos\psi)}{[(x_R-R\cos\psi-L\sin\chi)^2+(y_R-R\sin\psi)^2+(z_R+L\cos\chi)^2]^{3/2}} \tag{A40}$$

Axial vorticity.- For the axial vorticity, referring to figure A.4, the relevant quantities are found to be

$$\vec{s} = \vec{i}(L \sin \chi + R \cos \psi) + \vec{j}(R \sin \psi) + \vec{k}(-L \cos \chi) \tag{A41}$$

$$d\vec{s} = [\vec{i} \sin \chi - \vec{k} \cos \chi] dL \tag{A42}$$

$$\vec{r}-\vec{s} = \vec{i}(x_R - L \sin \chi - R \cos \psi) + \vec{j}(y_R - R \sin \psi) + \vec{k}(z_R + L \cos \chi) \tag{A43}$$

The form of the Biot-Savart Law for the axial vorticity is

$$d\vec{V} = \frac{1}{4\pi} \left(\frac{d\Gamma_a}{dR\psi}\right) \frac{ds \times (\vec{r}-\vec{s})}{|\vec{r}-\vec{s}|^3} \, d(R\psi) \tag{A44}$$

Substituting equations (A42), (A43), and (A33) into equation (A44), yields the equations for the induced velocities due to the axial vorticity as follows

$$U_a = \frac{R\sqrt{\mu^2+\lambda^2}}{4\pi} \int_0^{2\pi} \int_0^{\infty} \left(\frac{d\Gamma_c}{dL}\right) \frac{\{y_R\cos\chi-R\sin\psi\cos\chi\} \; dL d\psi}{[(x_R-L\sin\chi-R\cos\psi)^2+(y_R-R\sin\psi)^2+(z_R+L\cos\chi)^2]^{3/2}} \tag{A45}$$

$$V_a = \frac{R\sqrt{\mu^2+\lambda^2}}{4\pi} \int_0^{2\pi}\int_0^{\infty} \left(\frac{d\Gamma_c}{dL}\right) \frac{\{-x_R\cos\chi+R\cos\psi\cos\chi-z_R\sin\chi\}\ dLd\psi}{[(x_R-L\sin\chi-R\cos\psi)^2+(y_R-R\sin\psi)^2+(z_R+L\cos\chi)^2]^{3/2}} \tag{A46}$$

$$W_a + \frac{R\sqrt{\mu^2+\lambda^2}}{4\pi} \int_0^{2\pi}\int_0^{\infty} \left(\frac{d\Gamma_c}{dL}\right) \frac{\{y_R\sin\chi-R\sin\psi\sin\chi\}\ dLd\psi}{[(x_R-L\sin\chi-R\cos\psi)^2+(y_R-R\sin\psi)^2+(z_R+L\cos\chi)^2]^{3/2}} \tag{A47}$$

Inner Wake

The radial vorticity is distributed across the interior of the wake, as depicted in figure A.5. The strength of the radial vorticity is the derivative of the strength of the blade vorticity.

$$\frac{d}{d\psi}\left[\frac{d\Gamma}{dL}\right] = \frac{d\Gamma_1}{dL}\cos\psi \tag{A48}$$

Again, starting with the appropriate form of the Biot-Savart Law,

$$dV_r = \frac{1}{4\pi}\frac{d}{d\psi}\left(\frac{d\Gamma}{dL}\right)\frac{\vec{ds}\times(\vec{r}-\vec{s})}{|\vec{r}-\vec{s}|^3}\,dLd\psi \tag{A49}$$

the following relations are found from figure A.5.

$$\vec{s} = \vec{i}(r\cos\psi + L\sin\chi) + \vec{j}(r\sin\psi) + \vec{k}(-L\cos\chi) \tag{A50}$$

$$\vec{ds} = (\vec{i}\cos\psi + \vec{j}\sin\psi)dr \tag{A51}$$

$$\vec{r}-\vec{s} = \vec{i}(x_R - r\cos\psi - L\sin\chi) + \vec{j}(y_R - r\sin\psi) + \vec{k}(z_R + L\cos\chi) \tag{A52}$$

Substituting these relations into equation (A49) the following expressions for the velocity components induced by the radial vorticity.

$$U_r = \frac{1}{4\pi} \int_0^{2\pi} \int_0^R \int_0^\infty \frac{d}{d\psi} \frac{d\Gamma}{dL} \frac{\{z_R \sin\psi + L\sin\psi\cos\chi\}\ dL dr d\psi}{[(x_R - r\cos\psi - L\sin\chi)^2 + (y_R - r\sin\psi)^2 + (z_R + L\cos\chi)^2]^{3/2}} \tag{A53}$$

$$V_r = \frac{1}{4\pi} \int_0^{2\pi} \int_0^R \int_0^\infty \frac{d}{d\psi} \frac{d\Gamma}{dL} \frac{\{-z_R \cos\psi - L\cos\psi\}\ dL dr d\psi}{[(x_R - r\cos\psi - L\sin\chi)^2 + (y_R - r\sin\psi)^2 + (z_R + L\cos\chi)^2]^{3/2}} \tag{A54}$$

$$W_r = \frac{1}{4\pi} \int_0^{2\pi} \int_0^R \int_0^\infty \frac{d}{d\psi} \frac{d\Gamma}{dL} \frac{\{y_R \cos\psi - x_R \sin\psi + L\sin\chi\sin\psi\}\ dL dr d\psi}{[(x_R - r\cos\psi - L\sin\chi)^2 + (y_R - r\sin\psi)^2 + (z_R + L\cos\chi)^2]^{3/2}} \tag{A55}$$

The above derivations express each of the velocity components in terms of integral relations for each of the four vortex systems. The next step is to integrate each of these integral relations.

INTEGRATION OF THE VORTEX EQUATIONS

For each of the three components of induced velocity there are four terms, due to

1) Root vorticity; U_R, V_R, W_R
2) Circumferential vorticity; U_c, V_c, W_c
3) Axial vorticity; U_a, V_a, W_a
4) Radial vorticity; U_r, V_r, W_r

Each of the total of twelve terms has been expressed above in integral form involving single, double, or even triple integrals. In this section these terms are reduced to integrals over ψ, the azimuth angle, or, for the case of the root vorticity which is not a function of ψ, integrated completely. The remaining integrals over ψ are then solved numerically.

Root Vorticity

Integrating first the root vorticity terms, equation (A22) can be written

$$U_R = \frac{-b\Gamma_o y_R \cos\chi}{4\pi} \int_o^\infty \frac{dL}{[(x_R - L\sin\chi)^2 + y_R^2 + (z_R - L\cos\chi)^2]^{3/2}} \qquad (A56)$$

Expanding the denominator of this integrand and expressing it in the form $R_I = a + bL + cL^2$ reduces equation (A56) to the general form

$$\int \frac{dL}{\sqrt{R_I^3}}$$

The solution to this integral can be found in reference A.2 (integral 2.264, no. 5) and is

$$\int \frac{dL}{\sqrt{R_I^3}} = \frac{2(2cL + b)}{\Delta\sqrt{R_I}} \qquad (A57)$$

where

$$\Delta = 4ac - b^2 \qquad (A58)$$

Applying this solution to equation (A56) and evaluating the result at the limits yields

$$U_R = \frac{-b\Gamma_o y_R \cos\chi}{4\pi} \left\{ \frac{1 + (x_R\sin\chi + z_R\cos\chi)/R_P}{[R_P^2 - x_R^2\sin^2\chi - z_R^2\cos^2\chi - x_R z_R \sin\chi\cos\chi]} \right\} \qquad (A59)$$

where $R_P^2 = x_R^2 + y_R^2 + z_R^2$ and is the distance from the origin of coordinates (the center of the rotor) to the field point $P(x_R, y_R, z_R)$.

The relation for V_R is given by equation (A23) and is

$$V_R = \frac{-b\Gamma_o}{4\pi} \int_o^\infty \frac{-\sin\chi(z_R-L\cos\chi)-\cos\chi(y_R-L\sin\chi)}{[(x_R-L\sin\chi)^2+y_R^2+(z_R-L\cos\chi)^2]^{3/2}}\, dL \qquad (A60)$$

The denominator is the same as in equation (A56). Expanding the numerator shows there are three terms, the first two independent of L and the third term varies with L to the first power. Hence, the first two terms can make use of the solution for U_R and the third term is of the general form

$$\int \frac{LdL}{\sqrt{R_I^3}}$$

The solution to this integral is given by integral 2.264, no. 6 of reference A.2;

$$\int \frac{LdL}{\sqrt{R_I^3}} = \frac{-2(2a + bL)}{\Delta\sqrt{R_I}} \qquad (A61)$$

Applying equations (A57) and (A61) to equation (A60) and evaluating the result at the limits yields the following relation for V_R.

$$V_R = \frac{-b\Gamma_o}{4\pi} \left\{ (-z_R \sin\chi - x_R \cos\chi) \left[\frac{1 + x_R \sin\chi + z_R \cos\chi)/R_P}{(\Delta/4)} \right] \right.$$

$$\left. + (2 \sin\chi \cos\chi) \left[\frac{R_P + x_R \sin\chi + z_R \cos\chi}{(\Delta/4)} \right] \right\} \qquad (A62)$$

The relation for W_R, given by equation (A24), is

$$W_R = \frac{-b\Gamma_o}{4\pi} \int_o^\infty \frac{y_R \sin\chi dL}{[(x_R-L\sin\chi)^2+y_R^2+(z_R-L\cos\chi)^2]^{3/2}} \qquad (A63)$$

The general form for this integral is the same as the general form for U_R. Thus the same general solution, given by equation (A57), can be used. Writing the final result directly,

$$W_R = \frac{-b\Gamma_o}{4\pi} y_R \sin\chi \left\{ \frac{1 + (x_R \sin\chi + z_R \cos\chi)/R_P}{[R_P^2 - x_R^2 \sin^2\chi - z_R^2 \cos^2\chi - x_R z_R \sin\chi\cos\chi]} \right\} \quad \text{(A64)}$$

Circumferential Vorticity

The x-component of the induced velocity due to the circumferential vorticity, given by equation (A38) is repeated here.

$$U_c = \frac{-R}{4\pi} \int_o^{2\pi} \int_o^{\infty} \left[\frac{d\Gamma_c}{dL}\right] \frac{(z_R + L\cos\chi)\cos\psi \; dL d\psi}{[(x_R - R\cos\psi - L\sin\chi)^2 + (y_R - R\sin\psi)^2 + (z_R + L\cos\chi)^2]^{3/2}} \quad \text{(A65)}$$

The denominator, grouped into powers of L, becomes

$$R_c^2 + 2(z_R \cos\chi - x_R \sin\chi + R\cos\psi \sin\chi)L + L^2 \quad \text{(A66)}$$

where

$$R_c^2 = R_P^2 + R^2 - 2R(x_R \cos\psi + y_R \sin\psi).$$

This quantity is the distance between the point on the rotor disc at the angle ψ and the field point $P(x_R, y_R, z_R)$ as shown in figure A.1. Recalling from equation (A32) that $(d\Gamma_c/dL)$ is independent of L, equation (A65) can be expressed in two terms as follows.

$$U_c = \frac{-R}{4\pi} \int_o^{2\pi} \left[\frac{d\Gamma_c}{dL}\right] z_R \cos\psi \int_o^{\infty} \frac{dL}{[R_c^2 + 2(z_R\cos\chi - x_R\sin\chi + R\cos\psi\sin\chi)L + L^2]^{3/2}} d\psi$$

$$- \frac{R}{4\pi} \int_o^{2\pi} \left[\frac{d\Gamma_c}{dL}\right] \cos\chi \cos\psi \int_o^{\infty} \frac{L dL}{[R_c^2 + 2(z_R\cos\chi - x_R\sin\chi + R\cos\psi\sin\chi)L + L^2]^{3/2}} d\psi \quad \text{(A67)}$$

Integrating over L by applying equations (A57) and (A61) the expression for U_c becomes

$$U_c = \frac{-R}{4\pi} \int_0^{2\pi} \left(\frac{d\Gamma_c}{dL}\right) \frac{\cos\psi (R_c\cos\chi + z_R)\, d\psi}{[R_c + z_R\cos\chi - x_R\sin\chi + R\cos\psi\sin\chi]R_c} \qquad \text{(A68)}$$

The remaining two velocity components due to the circumferential vorticity (V_c and W_c) are of the same general form as U_c. That is the integrals can be broken into two terms, one corresponding to equation (A57) and the other to equation (A61). The results of the integrations can thus be written directly.

$$V_c = \frac{-R}{4\pi} \int_0^{2\pi} \left(\frac{d\Gamma_c}{dL}\right) \frac{\sin\psi (z_R + R_c\cos\chi)\, d\psi}{[R_c + z_R\cos\chi - x_R\sin\chi + R\cos\psi\sin\chi]R_c} \qquad \text{(A69)}$$

$$W_c = \frac{-R}{4\pi} \int_0^{2\pi} \left(\frac{d\Gamma_c}{dL}\right) \frac{R + R_c\sin\chi\cos\psi - x_R\cos\psi - y_R\sin\psi\, d\psi}{[R_c + z_R\cos\chi - x_R\sin\chi + R\cos\psi\sin\chi]R_c} \qquad \text{(A70)}$$

Axial Vorticity

Velocity terms for the axial vorticity involve the same integrals as for the root and circumferential vorticity, equations (A57) and (A61). Hence, the final expressions for these forms are written without derivation. From equation (A45),

$$U_a = \frac{R\sqrt{\mu^2+\lambda^2}}{4\pi} \int_0^{2\pi} \left(\frac{d\Gamma_c}{dL}\right) \frac{\cos\chi (y_R - R\sin\psi)\, d\psi}{[R_c + \sin\chi (R\cos\psi - x_R) + z_R\cos\chi]R_c} \qquad \text{(A71)}$$

From equation (A46),

$$V_a = \frac{R\sqrt{\mu^2+\lambda^2}}{4\pi} \int_0^{2\pi} \left(\frac{d\Gamma_c}{dL}\right) \frac{\cos\chi (R\cos\psi - x_R) - z_R\sin\chi\, d\psi}{[R_c + \sin\chi (R\cos\psi - x_R) + z_R\cos\chi]R_c} \qquad \text{(A72)}$$

From equation (A47),

$$W_a = \frac{R\sqrt{\mu^2+\lambda^2}}{4\pi} \int_0^{2\pi} \left(\frac{d\Gamma_c}{dL}\right) \frac{\sin\chi(y_R - R\sin\psi)\, d\psi}{[R_c + \sin\chi(R\cos\psi - x_R) + z_R\cos\chi]R_c} \qquad \text{(A73)}$$

Radial Vorticity

These terms, given by equations (A53), (A54), and (A55) involve integrals over both L and r. Integration over L involves the same general forms as the previous integrals over L. The integration with respect to r is somewhat more involved. The general forms of this integration is given in reference A.3 and is not repeated here. The final forms are, from equations (A53), (A54), and (A55),

$$U_r = \frac{-1}{4\pi} \int_0^{2\pi} \frac{d}{d\psi} \left(\frac{d\Gamma}{dL}\right) \left\{ \frac{2\sin\chi\sin^2\psi}{1-\sin^2\chi\cos^2\psi} \right.$$

$$\times \tan^{-1} \left[\frac{C(R_c - R_p - R)(1-\sin\chi\cos\psi)}{R_p(R_c-R)(1-\sin\chi\cos\psi)^2 + (A+B)(R_c+R_p-R)(1-\sin\chi\cos\psi) + (A+B)^2 + C^2} \right]$$

$$\left. - \frac{\sin\chi\cos\chi\sin\psi\cos\psi}{1-\sin^2\chi\cos^2\psi} \ln \left| \frac{R_c+B+R\sin\chi\cos\psi}{R_p+B} \right| - \frac{\cos\chi\sin\psi}{1-\sin^2\chi\cos^2\psi} \ln \left| \frac{R_c+A-R}{R_p+A} \right| \right\} d\psi \qquad \text{(A74)}$$

$$V_r = \frac{+1}{4\pi} \int_0^{2\pi} \frac{d}{d\psi} \left(\frac{d\Gamma}{dL}\right) \left\{ \frac{2\sin\chi\sin\psi\cos\psi}{1-\sin^2\chi\cos^2\psi} \right.$$

$$\times \tan^{-1} \left[\frac{C(R_c - R_p - R)(1-\sin\chi\cos\psi)}{R_p(R_c-R)(1-\sin\chi\cos\psi)^2 + (A\pm B)(R_c+R_p-R)(1-\sin\chi\cos\psi) + (A+B)^2 + C^2} \right]$$

$$\left. - \frac{\sin\chi\cos\chi\cos^2\psi}{1-\sin^2\chi\cos^2\psi} \ln \left| \frac{R_c+B+R\sin\chi\cos\psi}{R_p+B} \right| - \frac{\cos\chi\cos\psi}{1-\sin^2\chi\cos^2\psi} \ln \left| \frac{R_c+A-R}{R_p+A} \right| \right\} d\psi \qquad \text{(A75)}$$

$$W_r = \frac{+1}{4\pi} \int_0^{2\pi} \frac{d}{d\psi} \left(\frac{d\Gamma}{dL}\right) \Bigg\{ \frac{2\cos\chi}{1-\sin^2\chi\cos^2\psi}$$

$$\times \tan^{-1} \left[\frac{C(R_c-R_p-R)(1-\sin\chi\cos\psi)}{R_p(R_c-R)(1-\sin\chi\cos\psi)^2+(A+B)(R_c+R_p-R)(1-\sin\chi\cos\psi)+(A+B)^2+C^2} \right]$$

$$+ \frac{\sin^2\chi\sin\psi\cos\psi}{1-\sin^2\chi\cos^2\psi} \ln \left| \frac{R_c+B+R\sin\chi\cos\psi}{R_p+B} \right| + \frac{\sin\chi\sin\psi}{1-\sin^2\chi\cos^2\psi} \ln \left| \frac{R_c+A-R}{R_p+A} \right| \Bigg\} d\psi \tag{A76}$$

where

$$A = x_R \cos\psi + y_R \sin\psi \tag{A77}$$

$$B = z_R \cos\chi - x_R \sin\chi \tag{A78}$$

$$C = (y_R \cos\psi - x_R \sin\psi) \cos\chi - z_R \sin\chi \sin\psi \tag{A79}$$

As a final comment, some of the expressions derived above involve the number of blades, b. However, when the relations for the vortex strength are substituted into these relations the blade number drops out and the final expressions are independent of blade number, as discussed in the main text.

REFERENCES

A.1 Gessow, A. and Myers, G. C., Jr.: Aerodynamics of the Helicopter, Ungar Publishing Co., New York, (1967).

A.2 Gradshteyn, I. S. and Ryzhik, I. M.: Table of Integrals, Series, and Products, Academic Press, New York, (1965).

A.3 Heyson, H. H.: "Equations for the Induced Velocities near a Lifting Rotor with Nonuniform Azimuthwise Vorticity Distribution", NASA TN D-394, (1960).

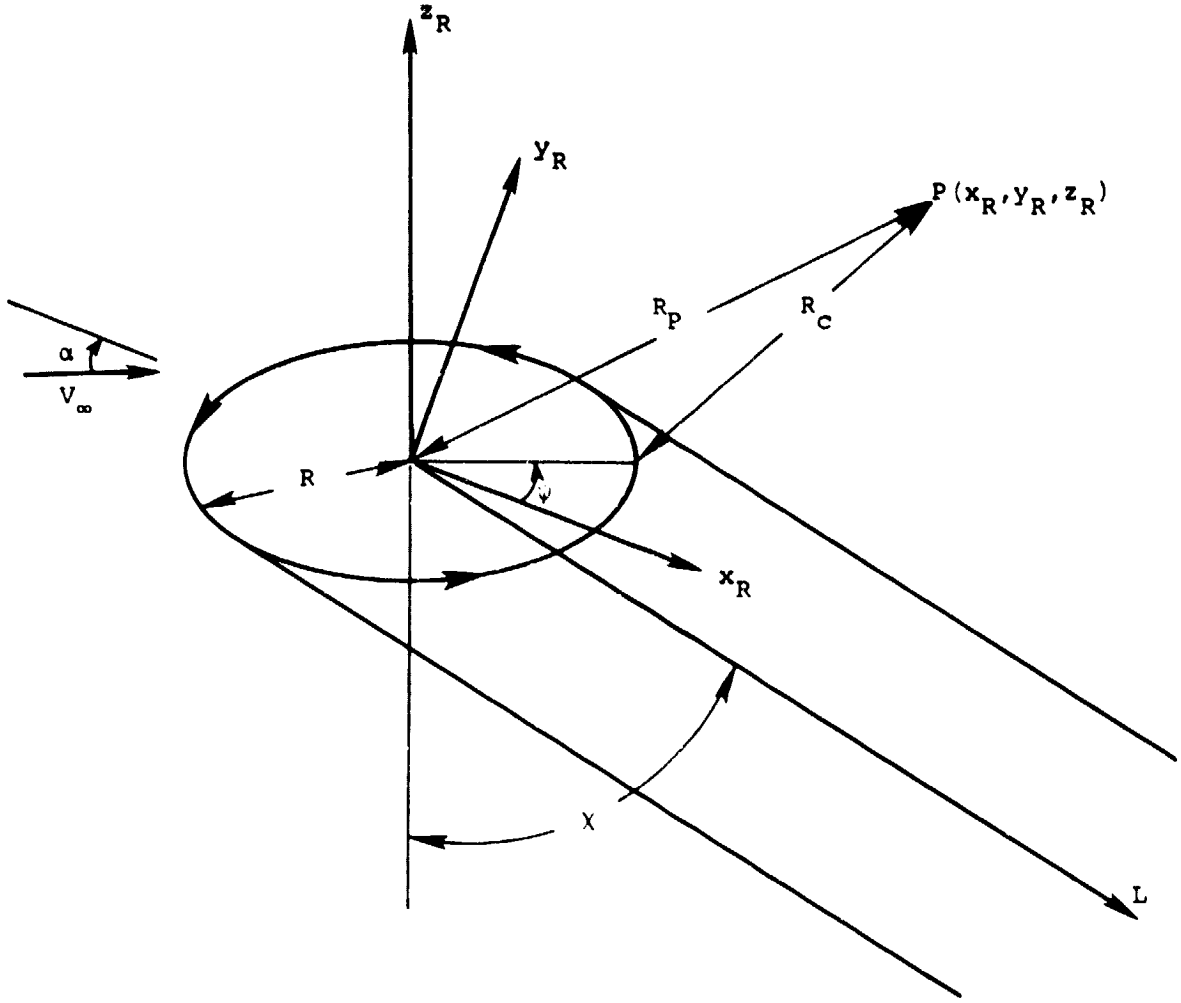

Figure A.1.- Rotor Wake Coordinate System

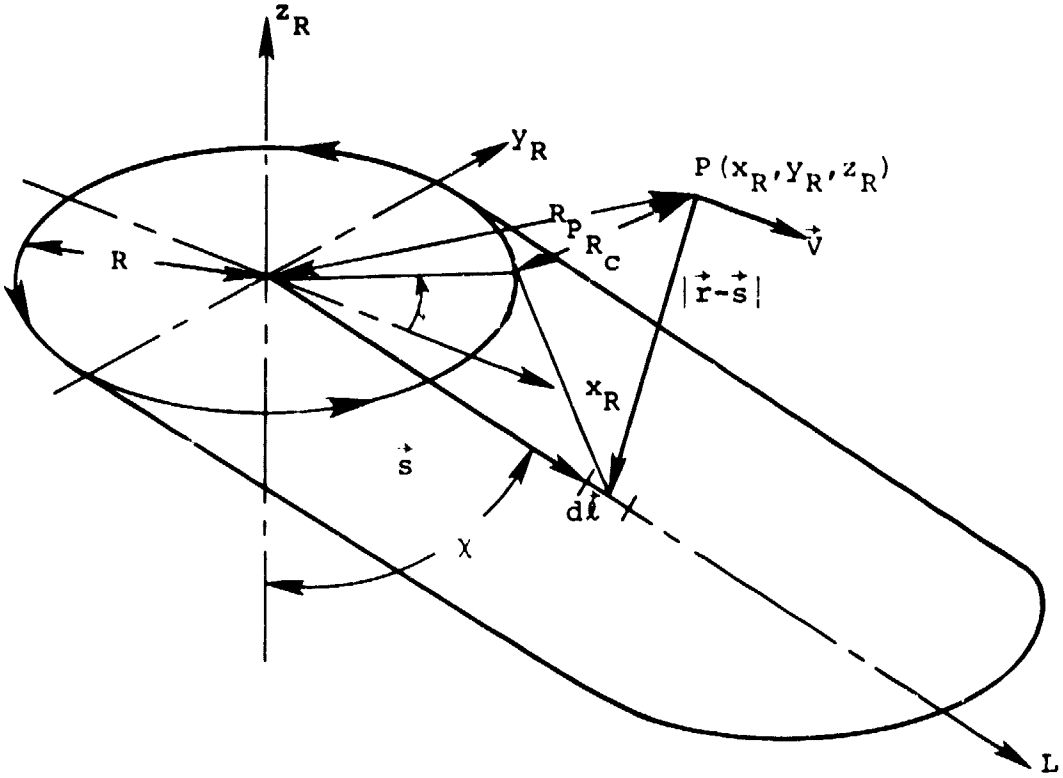

Figure A.2.- Root Vorticity Nomenclature

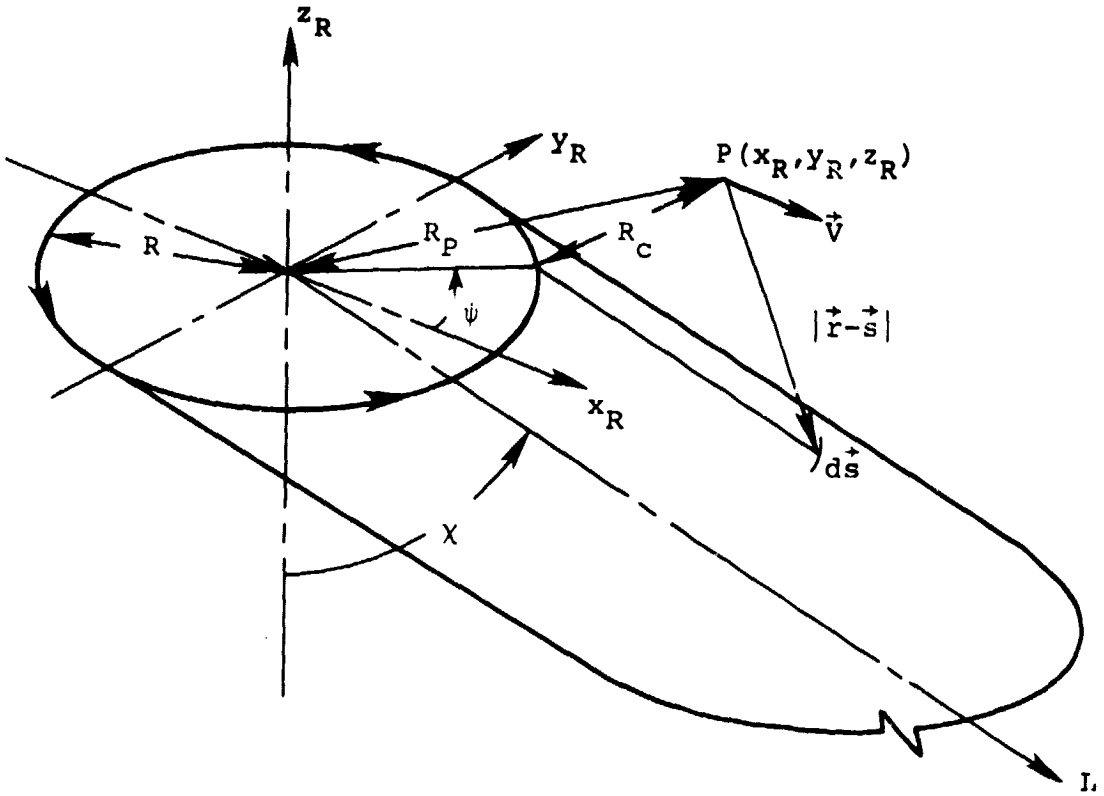

Figure A.3.- Outer Wake Circumferential Vorticity Nomenclature

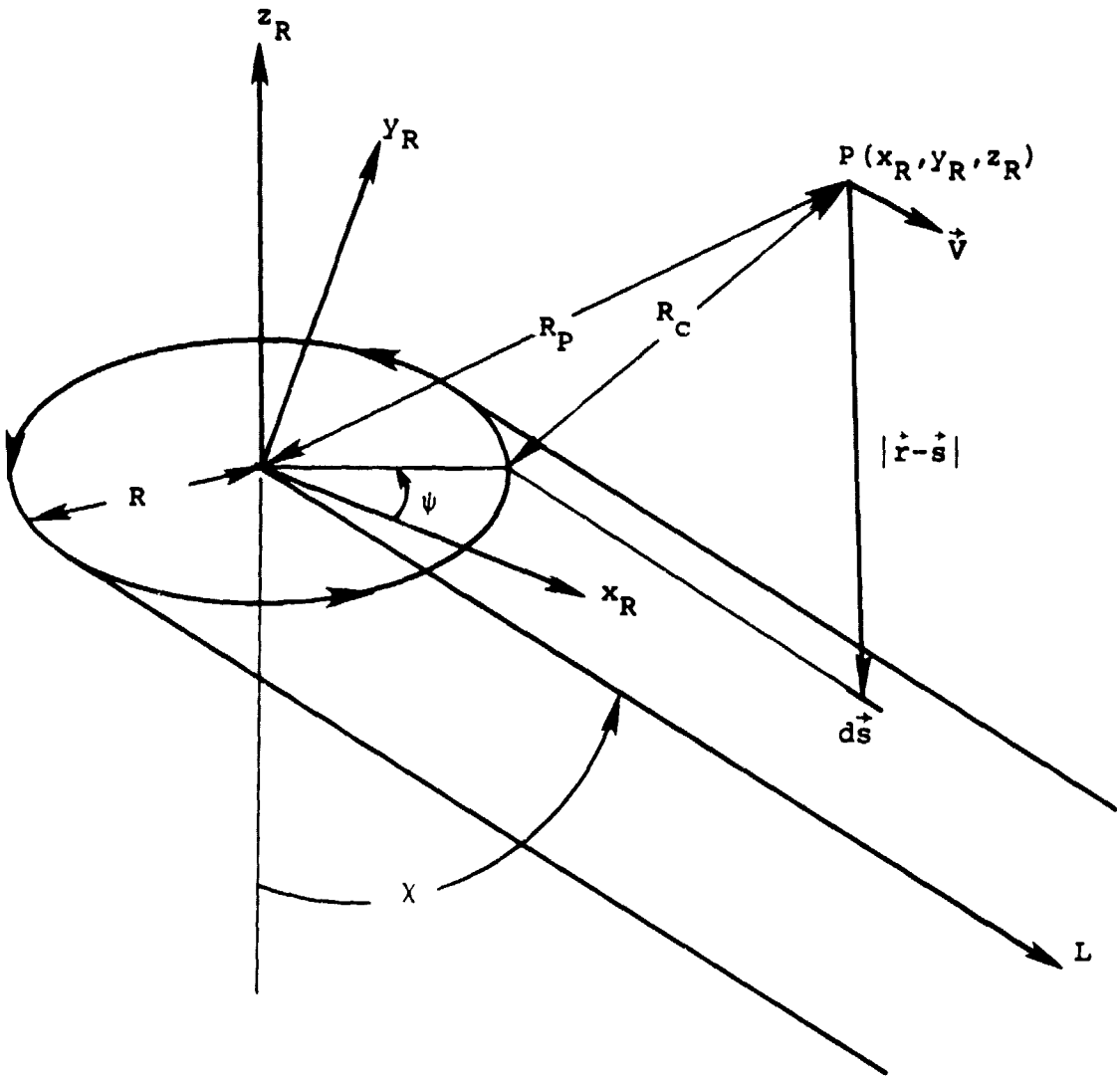

Figure A.4.- Outer Wake Axial Vorticity Nomenclature

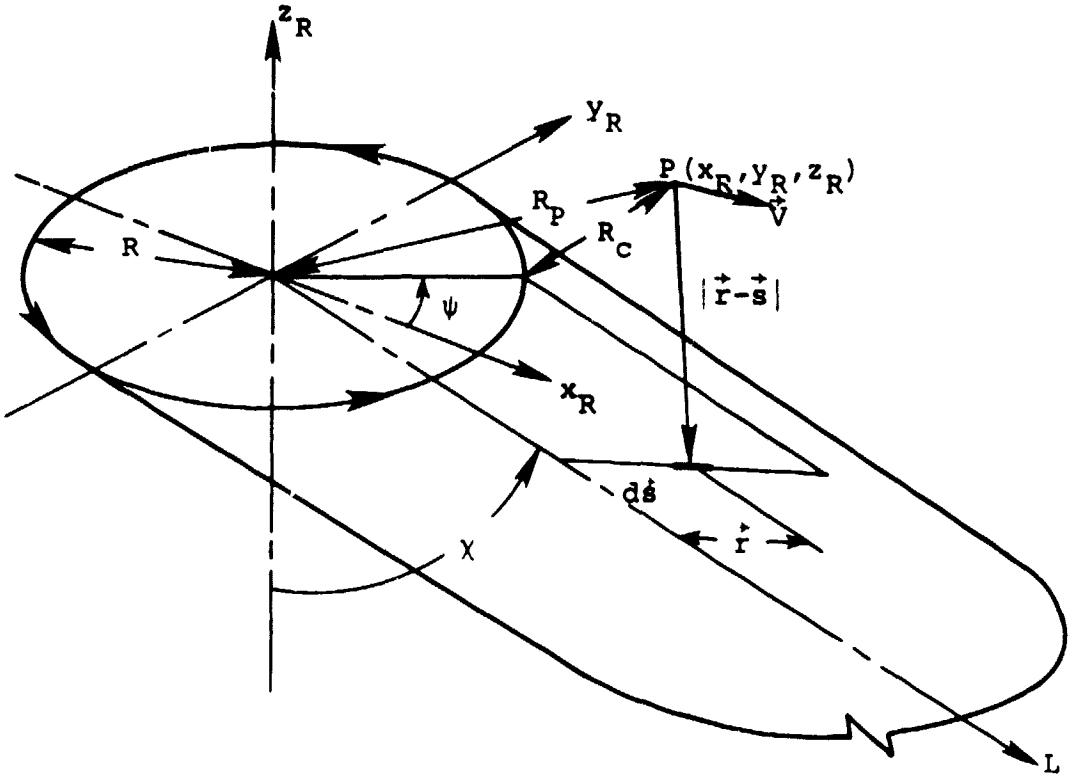

Figure A.5.- Inner Wake Radial Vorticity Nomenclature

REFERENCES

1. Goodyear Aerospace Corporation: Feasibility Study of Modern Airships. Phase II, Vol. I, Heavy Lift Airship Vehicle, NASA CR 151, 918, Sept. 1976.

2. Goodyear Aerospace Corporation: Feasibility Study of Modern Airships. Phase II, Vol. II, Airport Feeder Airship Vehicle, NASA CR 151, 920, Sept. 1976.

3. Goodyear Aerospace Corporation: Feasibility Study of Modern Airships. Vol. I, Book III, Aerodynamic Characteristics of Heavy Lift Airship as Measured at Low Speeds, NASA CR 151, 919, Sept. 1976.

4. Hess, R.: Calculation of Potential Flow About Arbitrary Three Dimensional Lifting Bodies. AD-755480, Oct. 1972.

5. Mack, D: Calculation of Potential Flow About Arbitrary Three Dimensional Lifting Bodies. Users Manual. AD-755933, Oct. 1972.

6. Heyson, H. H.: Equations for the Induced Velocities Near a Lifting Rotor with Nonuniform Azimuthwise Vorticity Distribution. NASA TN D-394. Aug. 1960.

7. Heyson, H. H.: A Note on the Mean Value of Induced Velocity for a Helicopter Rotor. NASA TN D-240, May 1960.

8. Kellogg, O. D.: Foundations of Potential Theory, Frederick Ungar Publishing Co. (1929). Also available through Dover Publications, Inc.

9. Hess, J. L. and Smith, A.M.O.: Calculation of Nonlifting Potential Flow About Arbitrary Three Dimensional Bodies. Douglas Aircraft Co., Report No. ES 40622, March 1962.

10. Cebeci, T., Mosinskis, G. J., and Smith, A.M.O.: Calculation of Viscous Drag and Turbulent Boundary Layer Separation on

Two Dimensional and Axisymmetric Bodies in Incompressible Flow. McDonnell Douglas Corp., Report MDC J0973-01, 1970.

11. Stratford, B. S.: The Prediction of Separation of the Turbulent Boundary Layer, J. Fluid Mech., Vol. 5, pp. 1-16, 1959.

12. Spangler, S. B. and Mendenhall, M. R.: Further Studies of Aerodynamic Loads at Spin Entry. Office of Naval Research, Report ONR-CR212-225-3, June 1977.

13. Carpenter, P. J.: Effect of Wind Velocity on Performance of Helicopter Rotors as Investigated with the Langley Helicopter Apparatus, NACA TN 1698, 1948.

14. Heyson, H. H. and Katzoff, S.: Induced Velocities Near a Lifting Rotor with Nonuniform Disk Loading, NACA Report 1319, 1957.

15. Mendenhall, M. R., Spangler, S. B., Nielsen, J. N. and Goodwin, F. K.: Calculation of the Longitudinal Aerodynamic Characteristics of Wing-Flap Configurations with Externally Blown Flaps. NASA CR-2705, 1976.

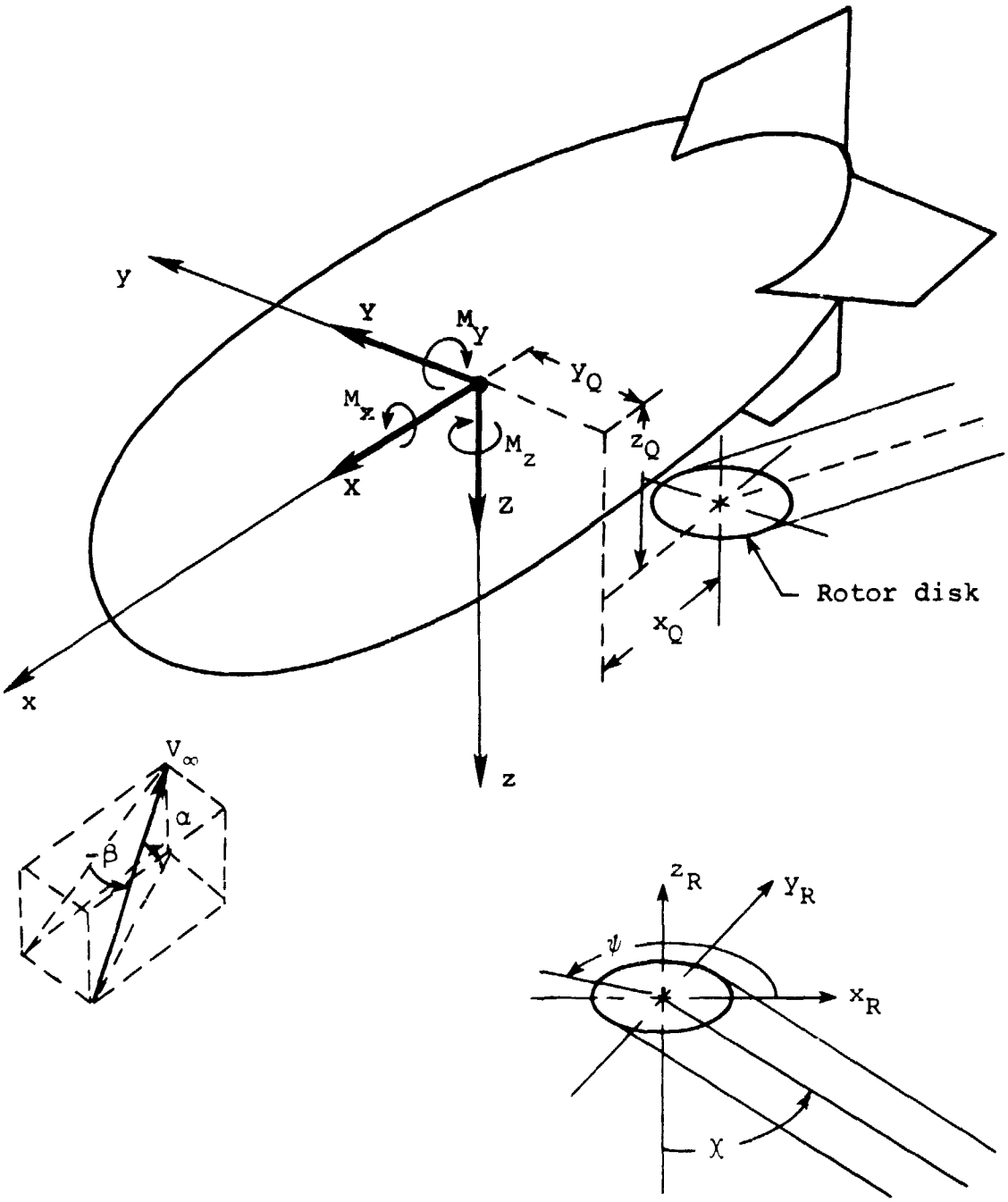

Figure 1.- Hull-rotor nomenclature.

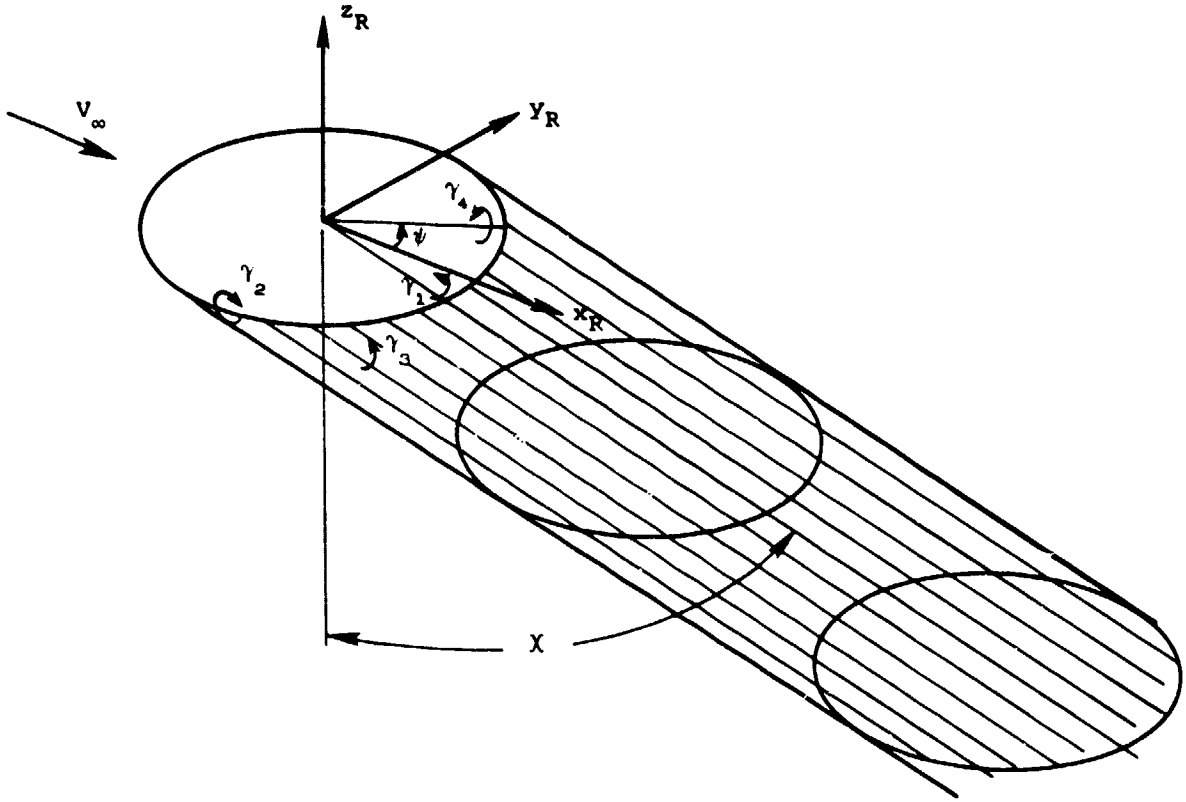

Figure 2.- Rotor model.

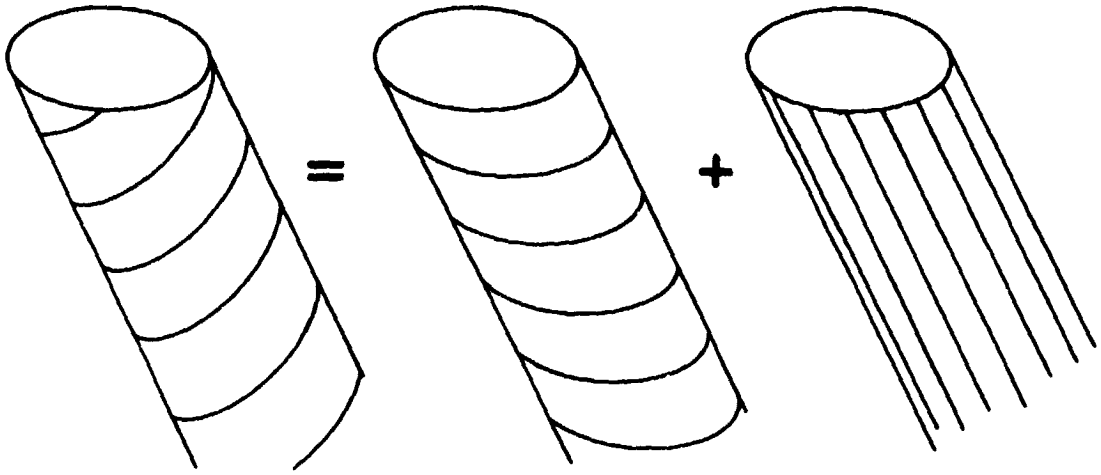

(a) Outer vortex wake. (b) Circumferential component. (c) Axial component.

Figure 3.- Decomposition of cylindrical wake into circumferential (vortex ring) and axial components (from reference 7).

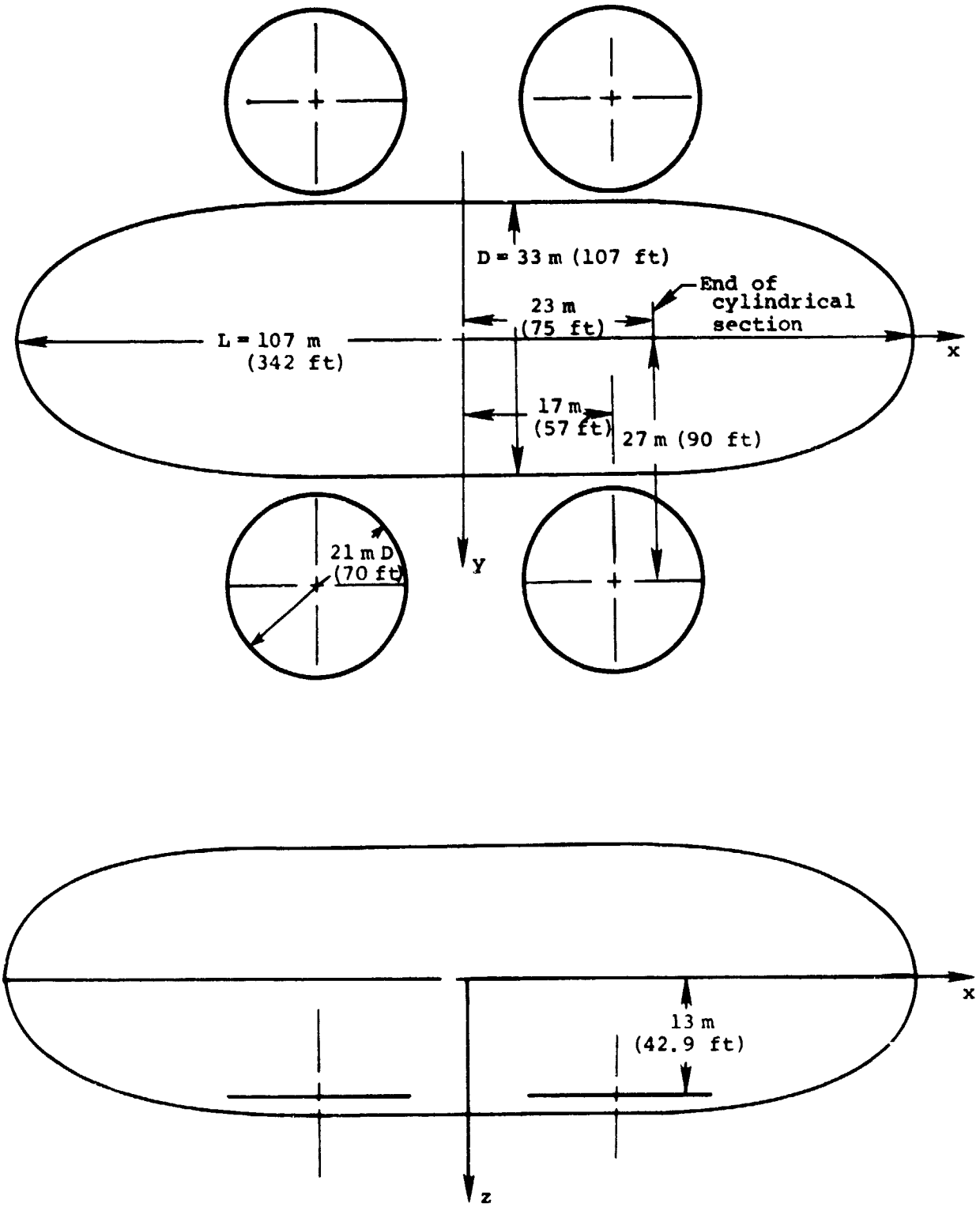

Figure 4.-Full scale HLA configuration

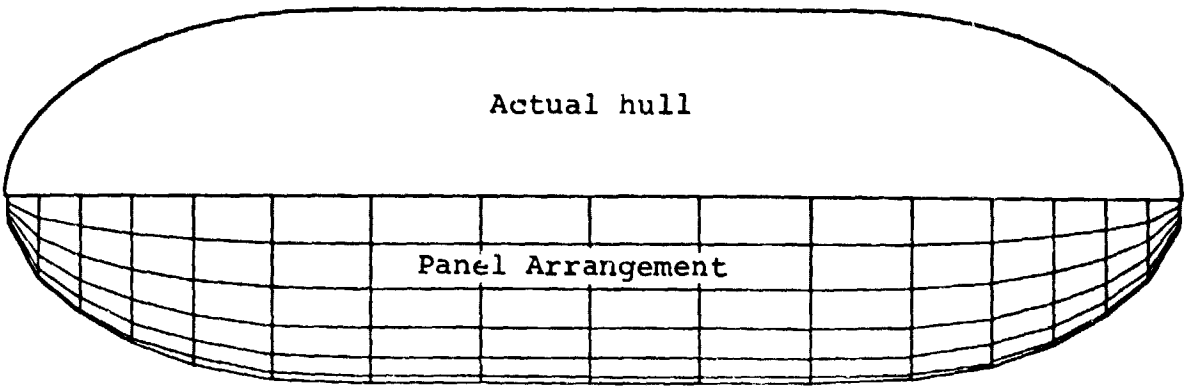

(a) Side view.

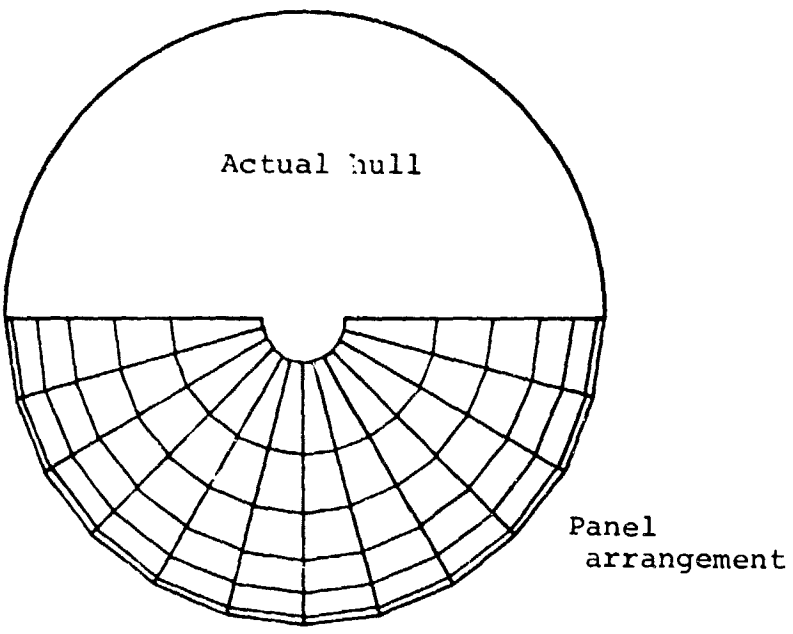

(b) End view.

Figure 5.- Panel arrangement on HLA hull.

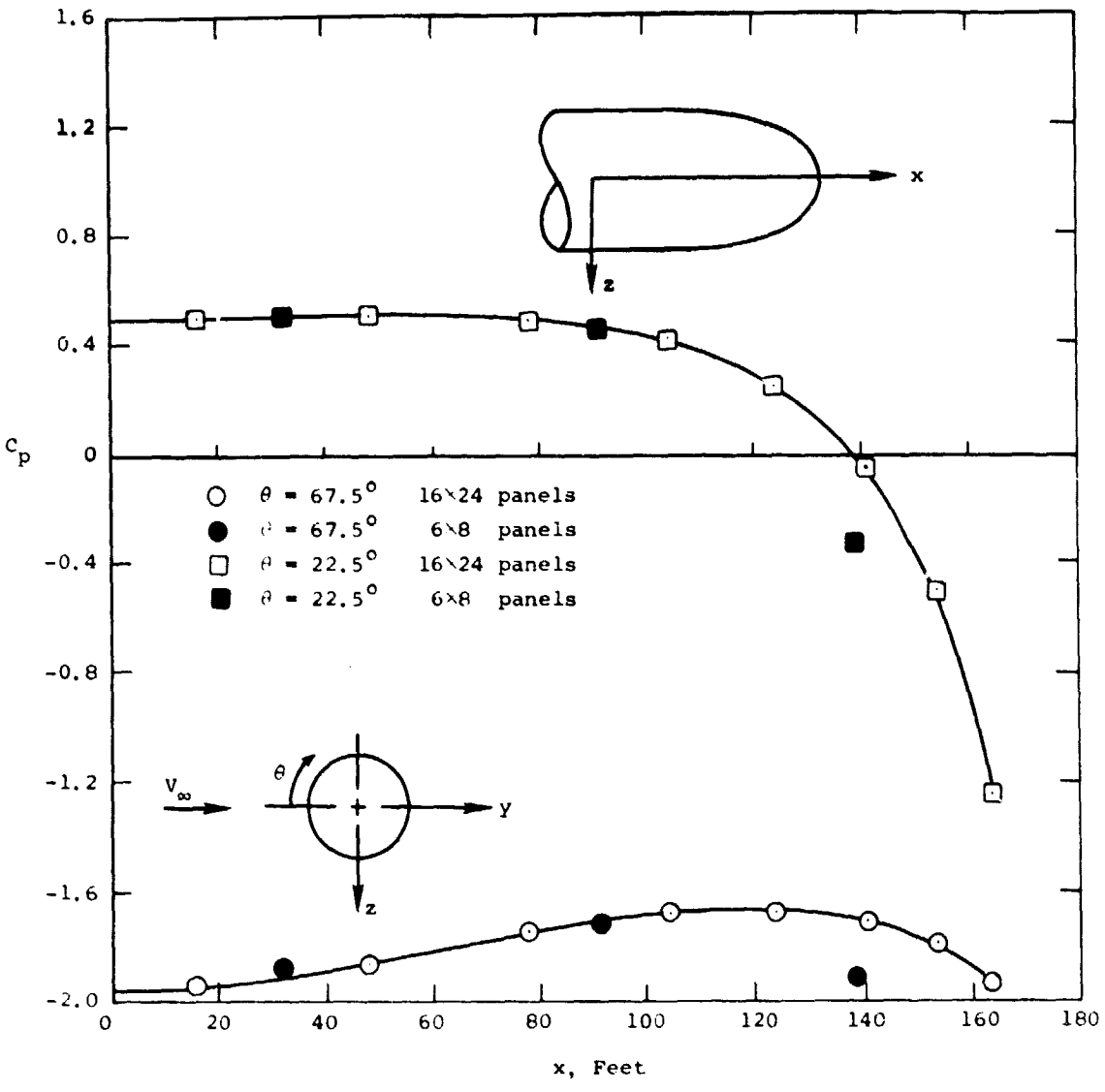

Figure 6.- Longitudinal pressure distributions on HLA hull alone at $\alpha = 0°$, $\beta = -90°$.

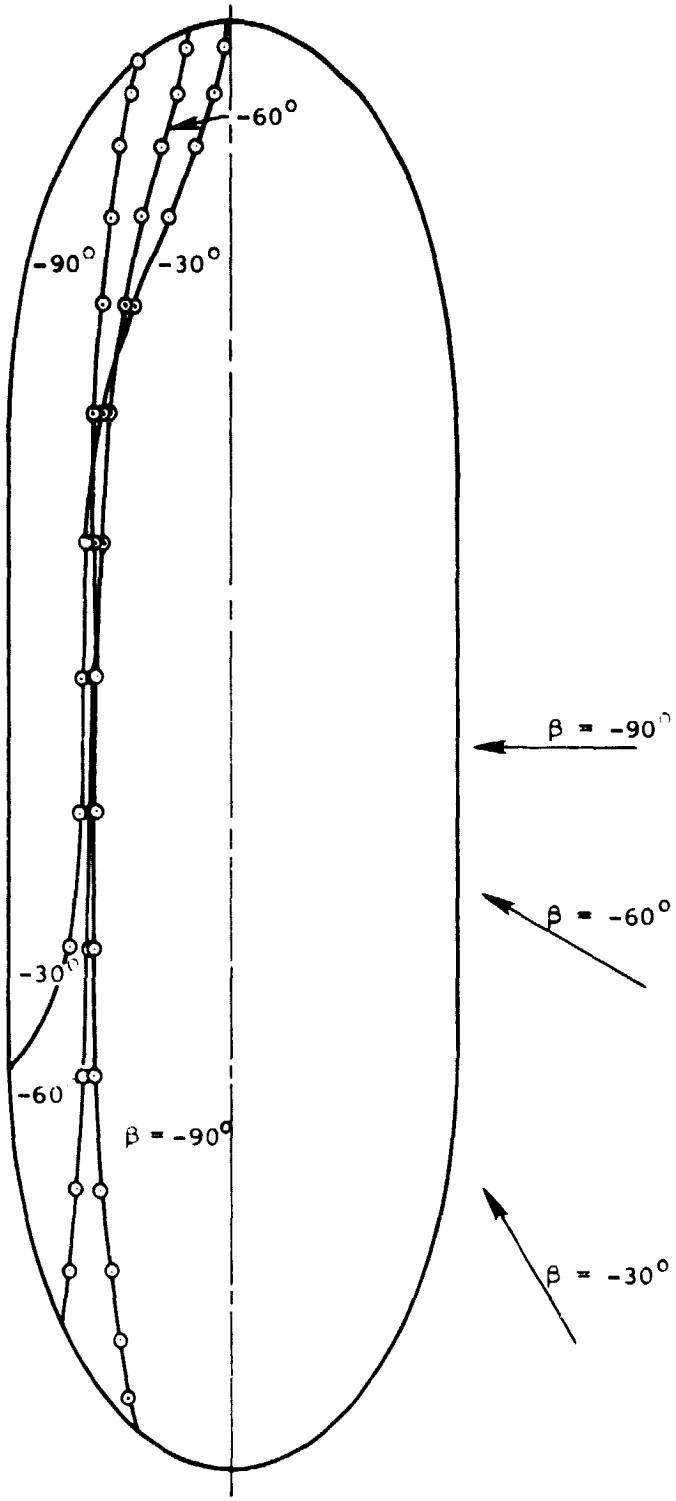

Figure 7.- Plan view of predicted seperation lines for various sideslip angles for HLA hull alone.

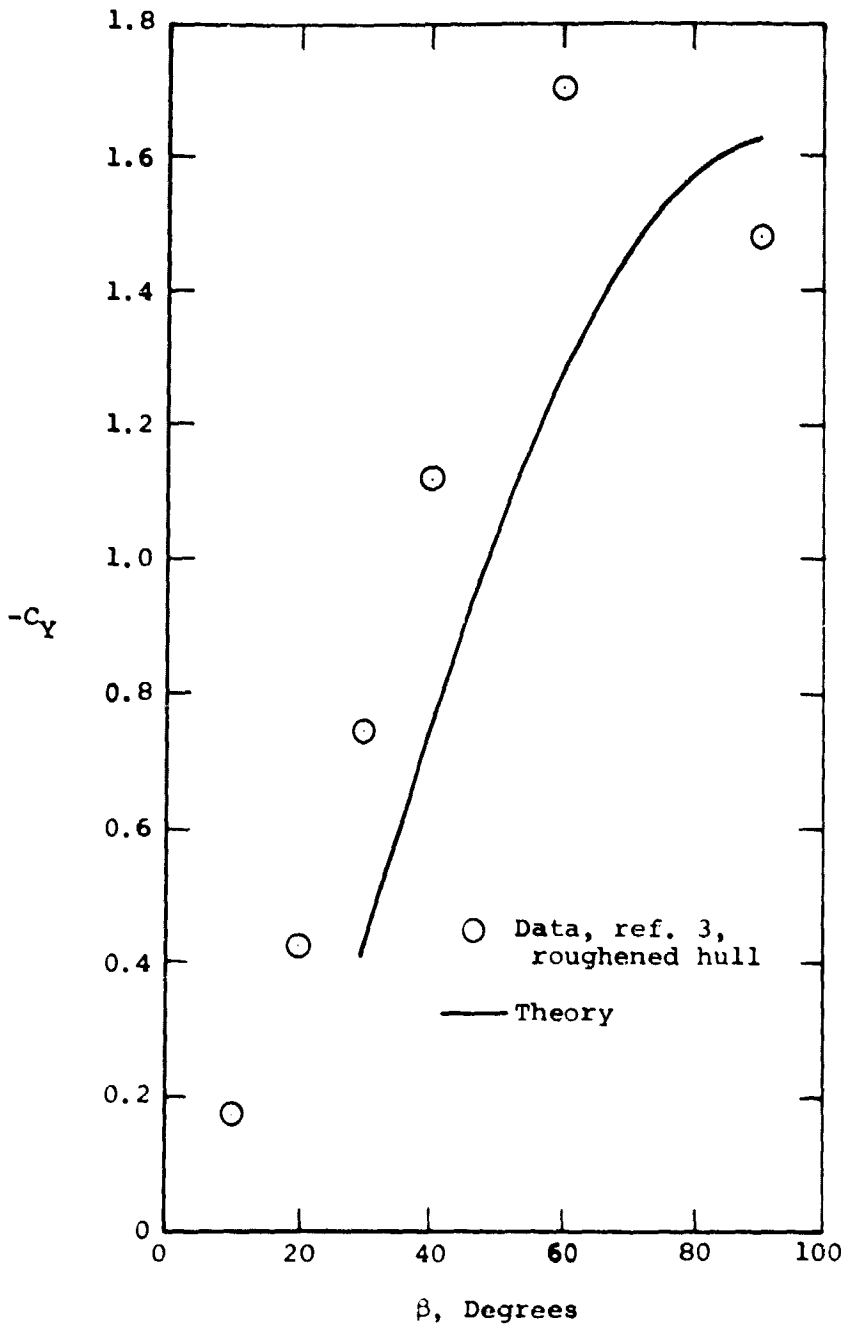

(a) Side force.

Figure 8.- Comparison of forces and moments for HLA hull alone out-of-ground effect.

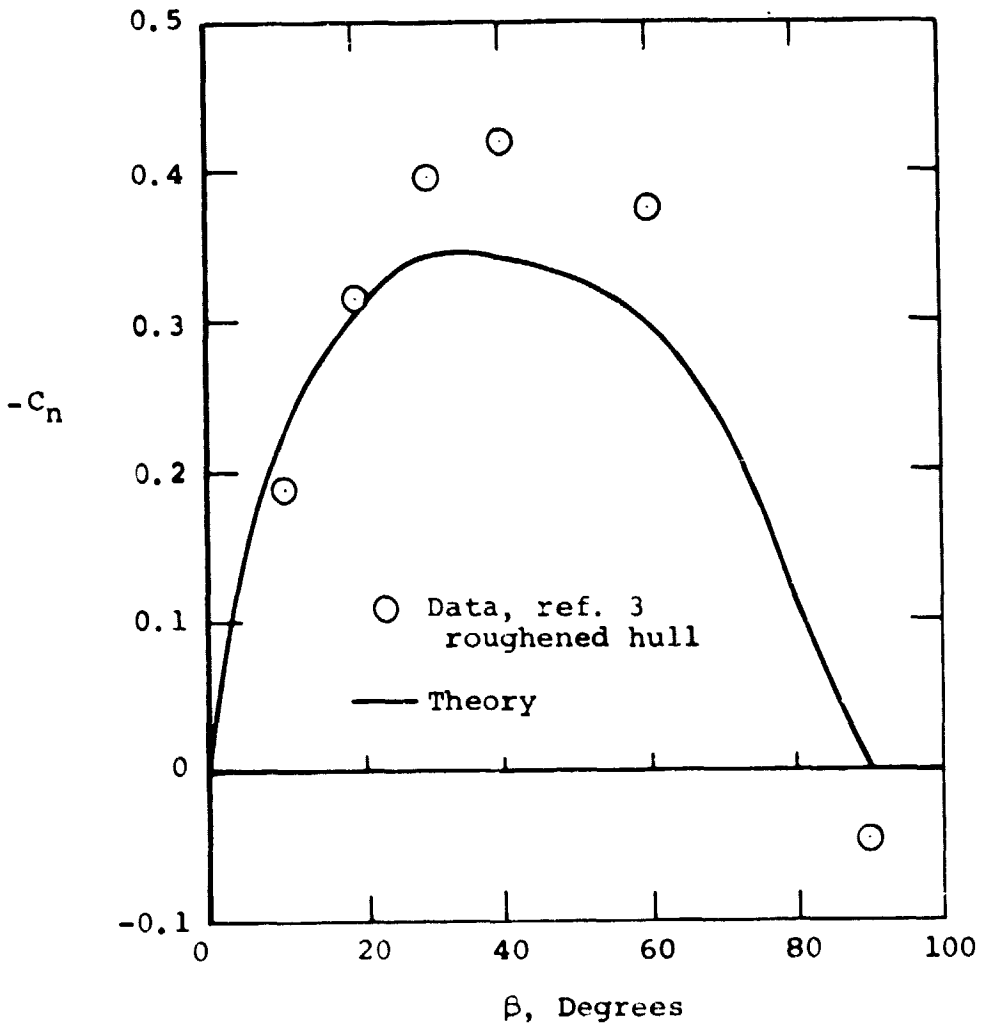

(b) Yawing moment.

Figure 8.- Concluded.

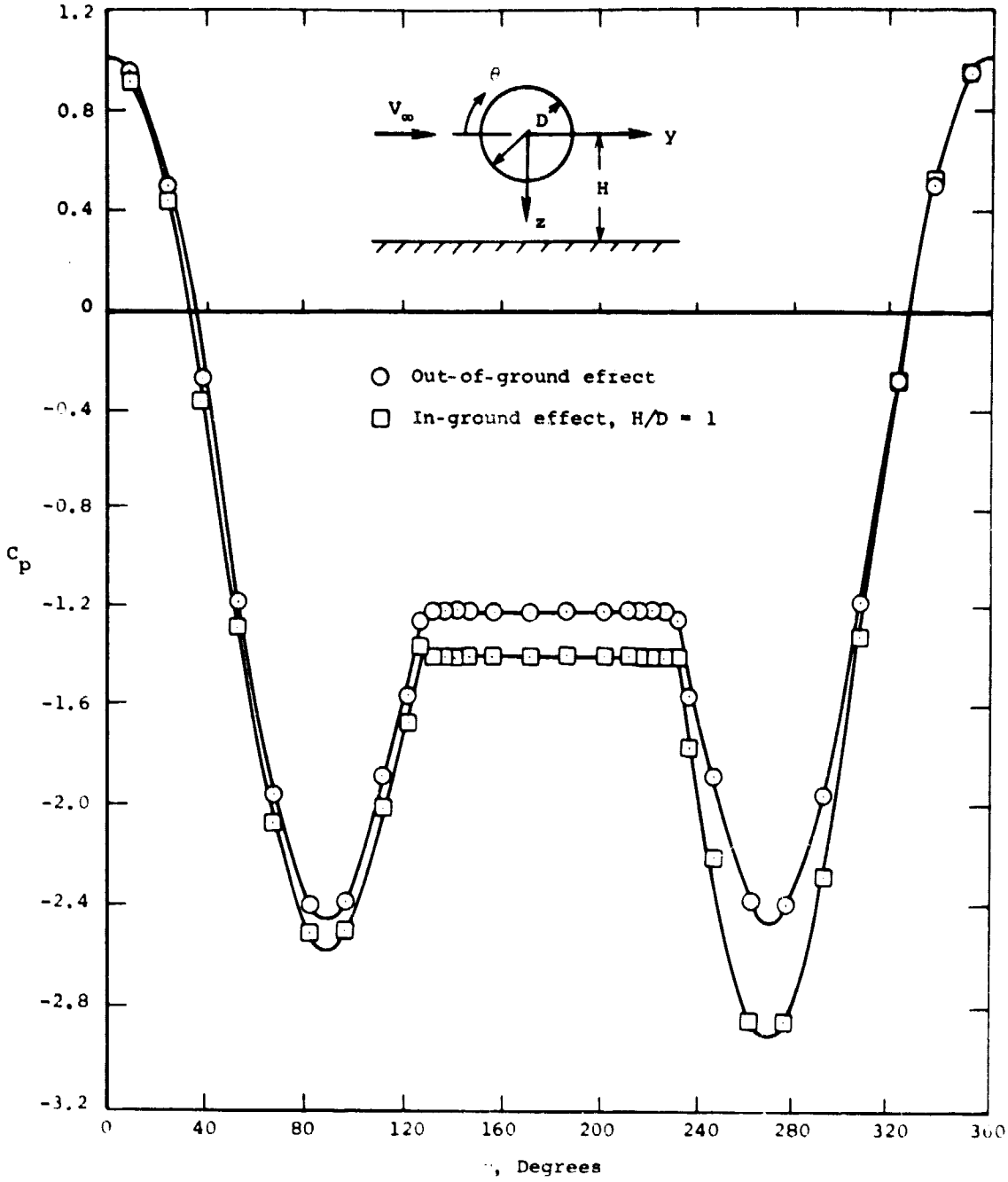

Figure 9.- Predicted circumferential pressure distribution near hull center (x = -5 m) for HLA hull alone at $\beta = -90^\circ$ in- and out-of-ground effect.

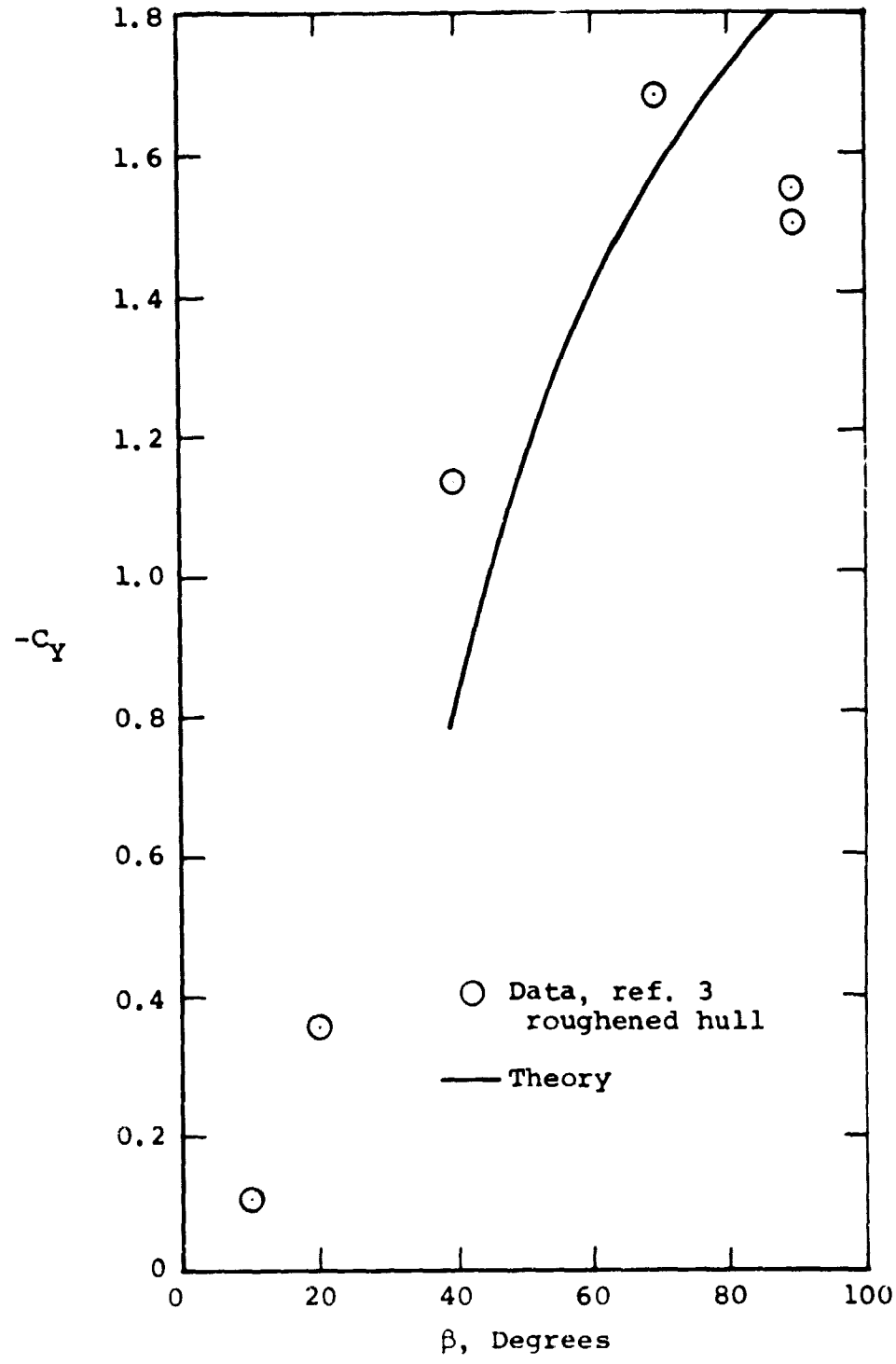

Figure 10.- Comparison of predicted and measured side force on HLA hull alone in ground effect. H/D = 1.

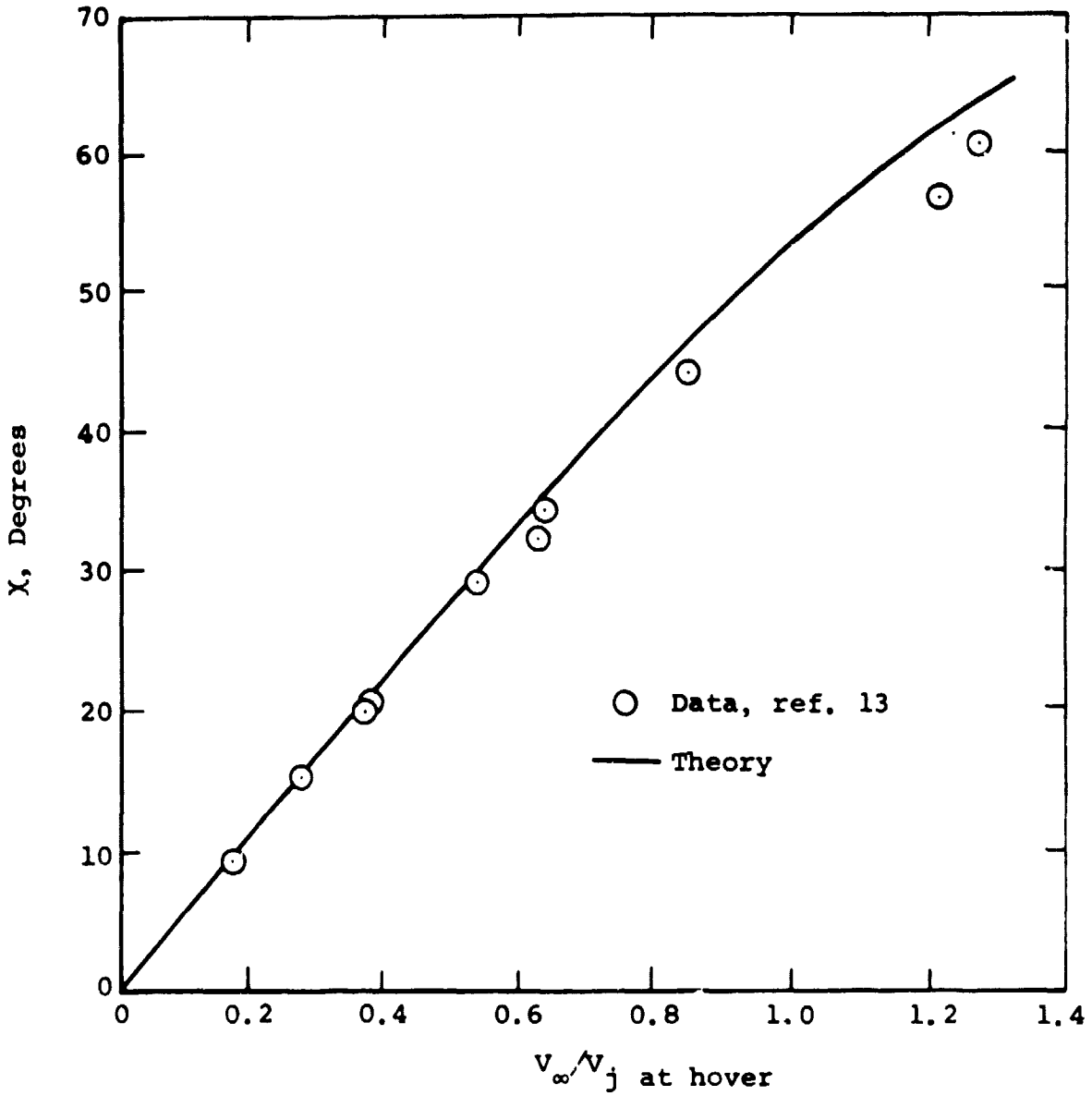

Figure 11.- Comparison of predicted and measured skew angles for a rotor alone.

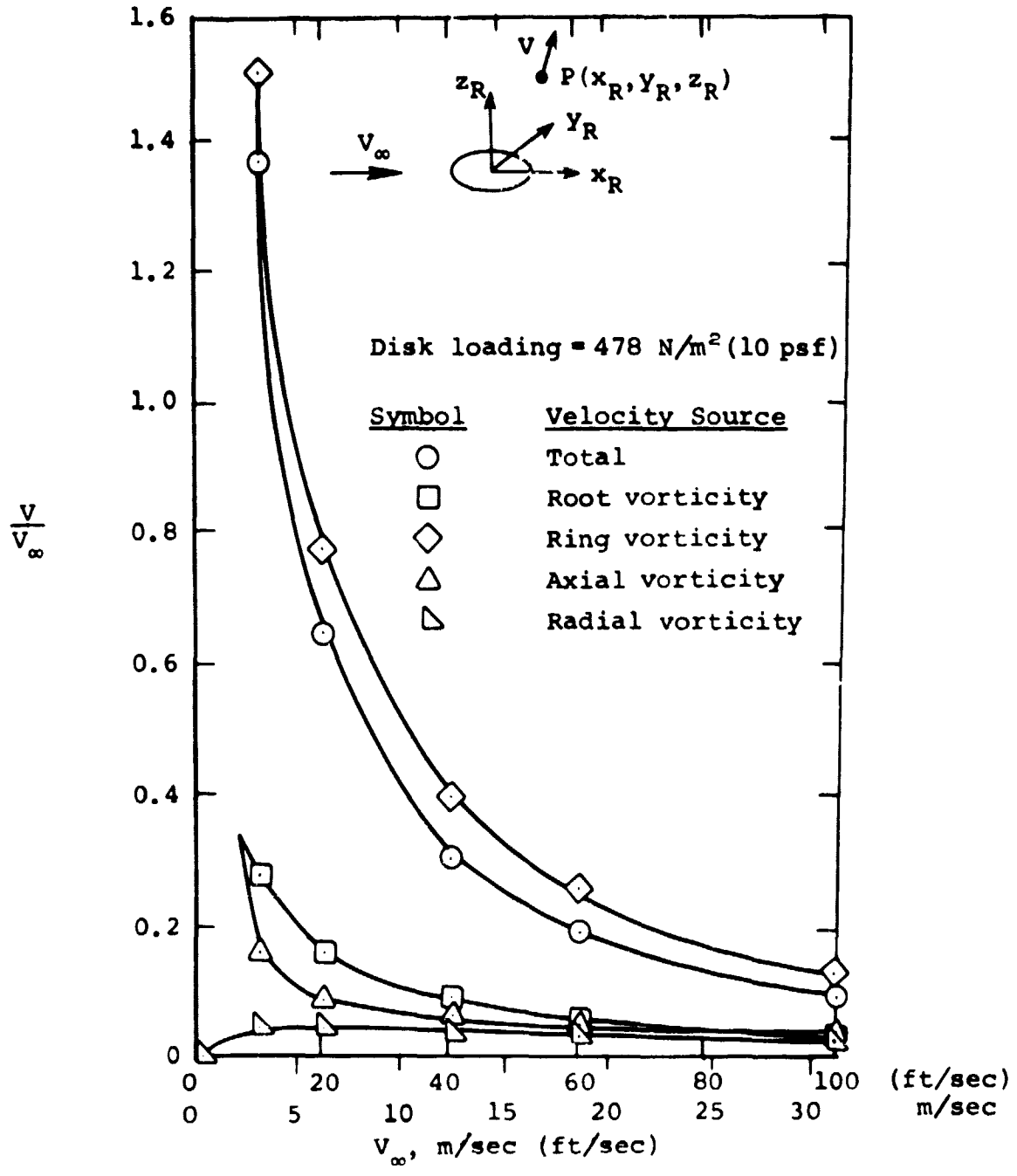

(a) Point in near field (0.25 R, -1.33 R, 0.3 R).

Figure 12.- Magnitude of induced velocity contributions at a point outside the wake for vortex systems comprising a rotor alone in a uniform flow.

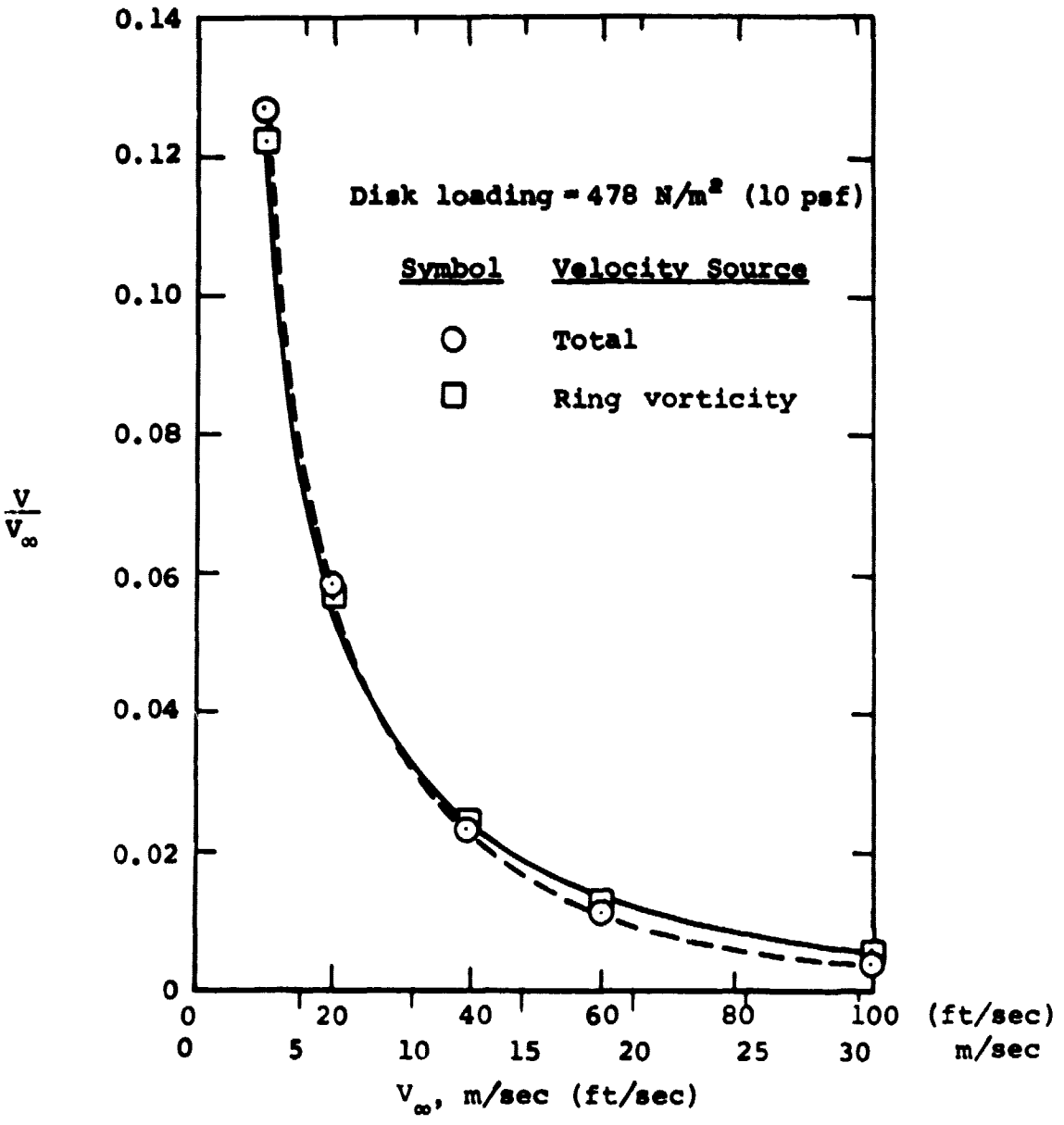

(b) Point in far field
(-2.99 R, -2.44 R, 1.64 R).

Figure 12.- Concluded.

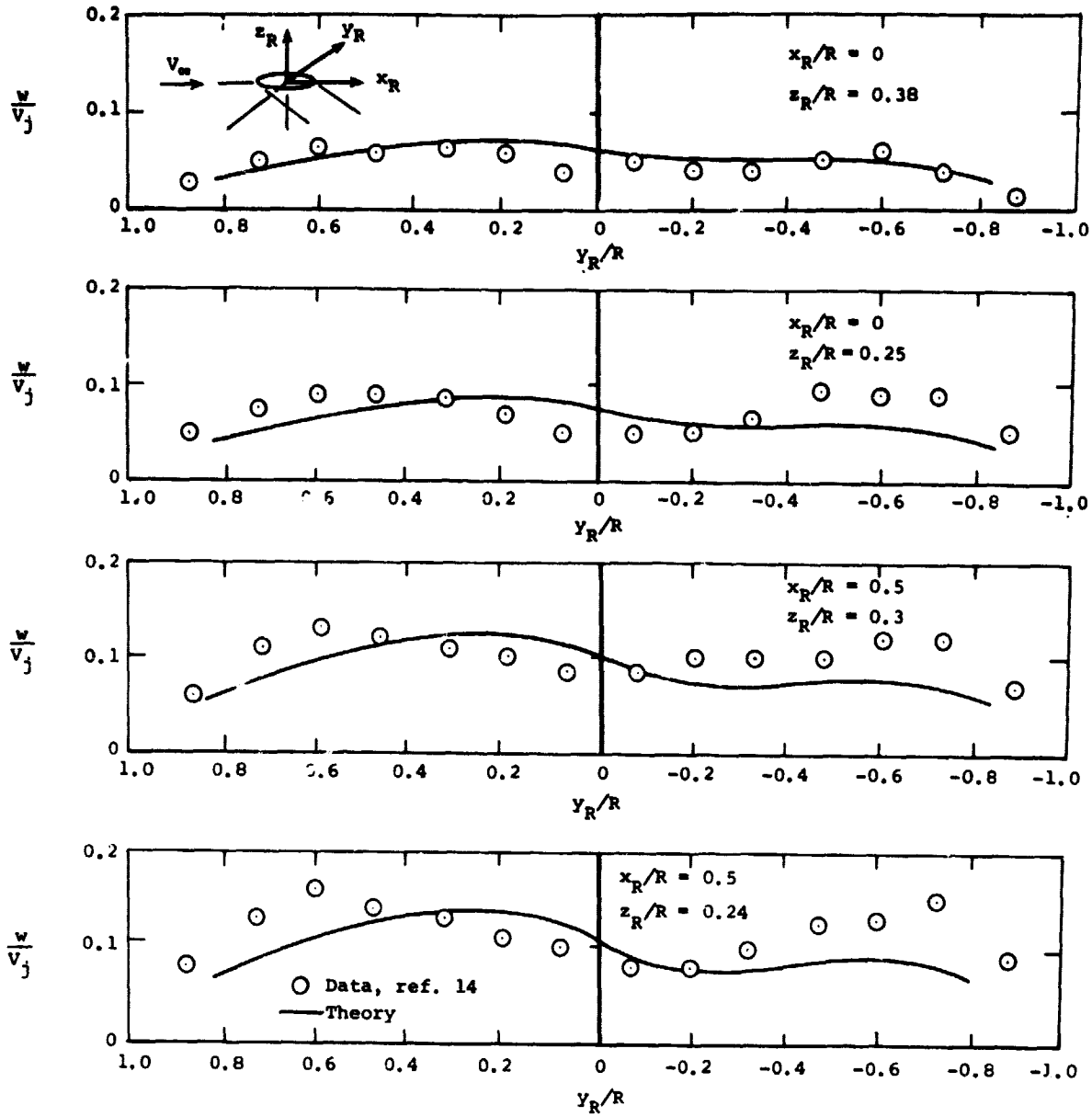

Figure 13.- Comparison of measured and predicted vertical-induced velocity for a rotor alone in a uniform flow at $V_j/V_\infty = 0.167$.

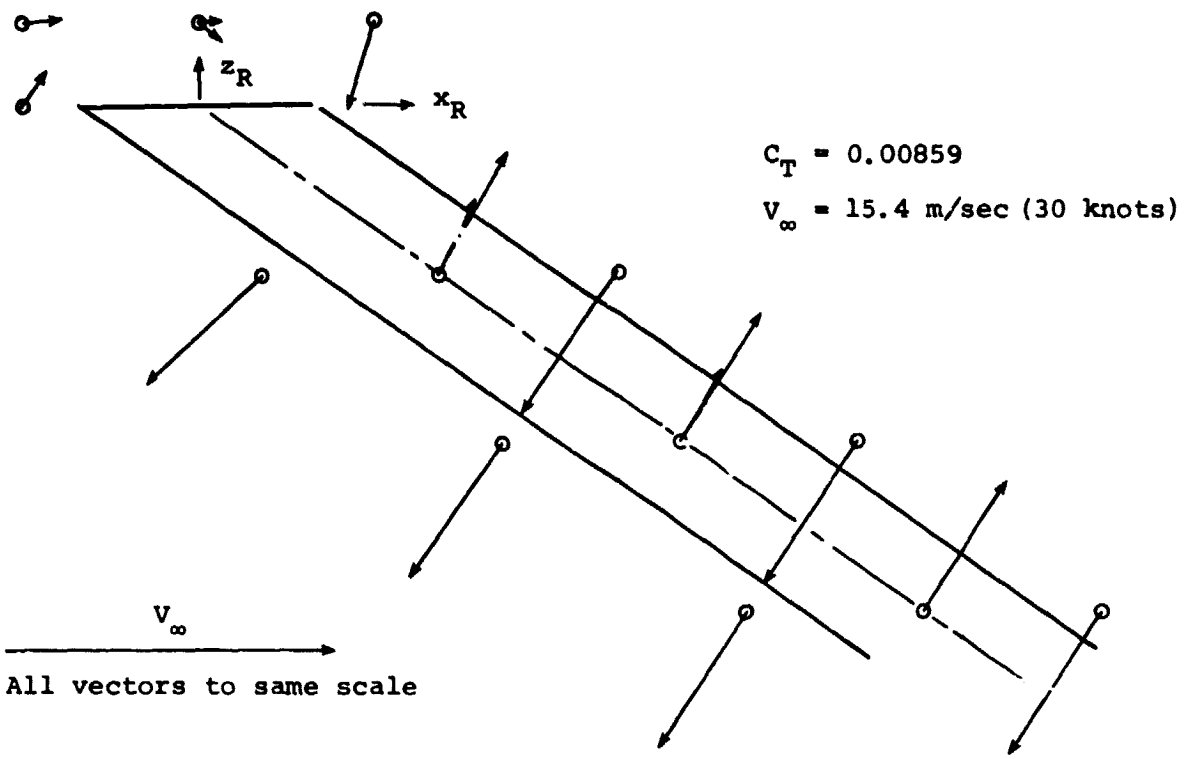

(a) Side view.

Figure 14.- Induced velocities adjacent to a rotor in a uniform flow.

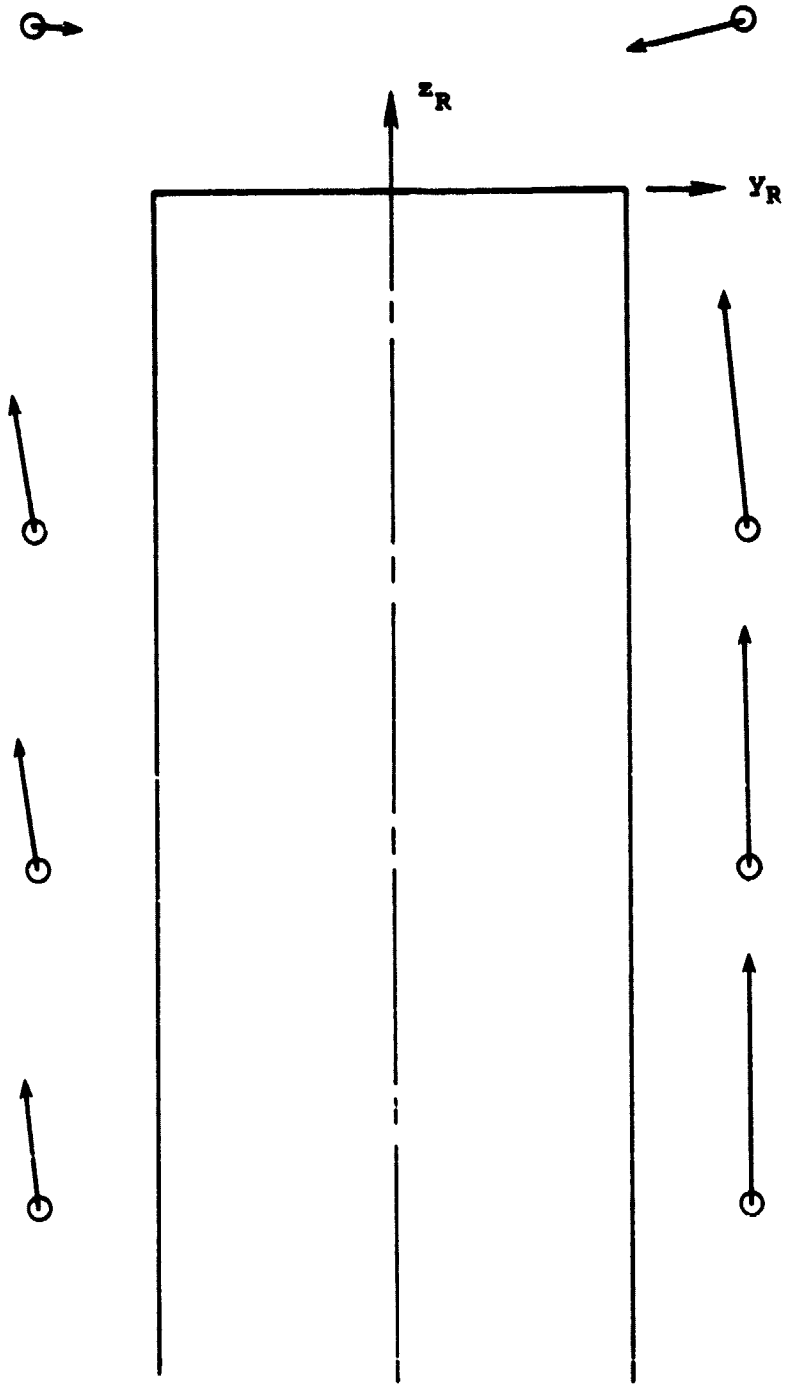

(b) View looking upstream.

Figure 14.- Concluded.

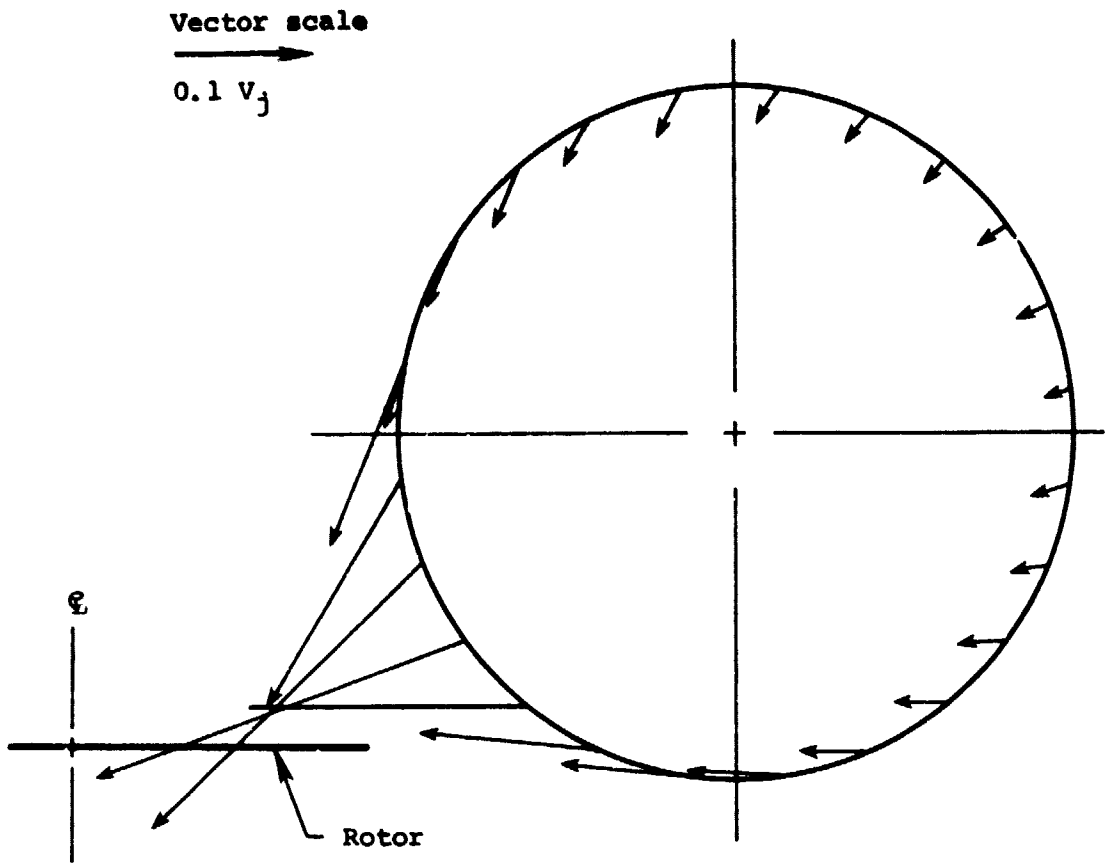

Figure 15.- Rotor-induced velocities on HLA hull in hover at x = 15 m (48 ft). T_4/S_R = 395 N/m^2 (8.26 psf).

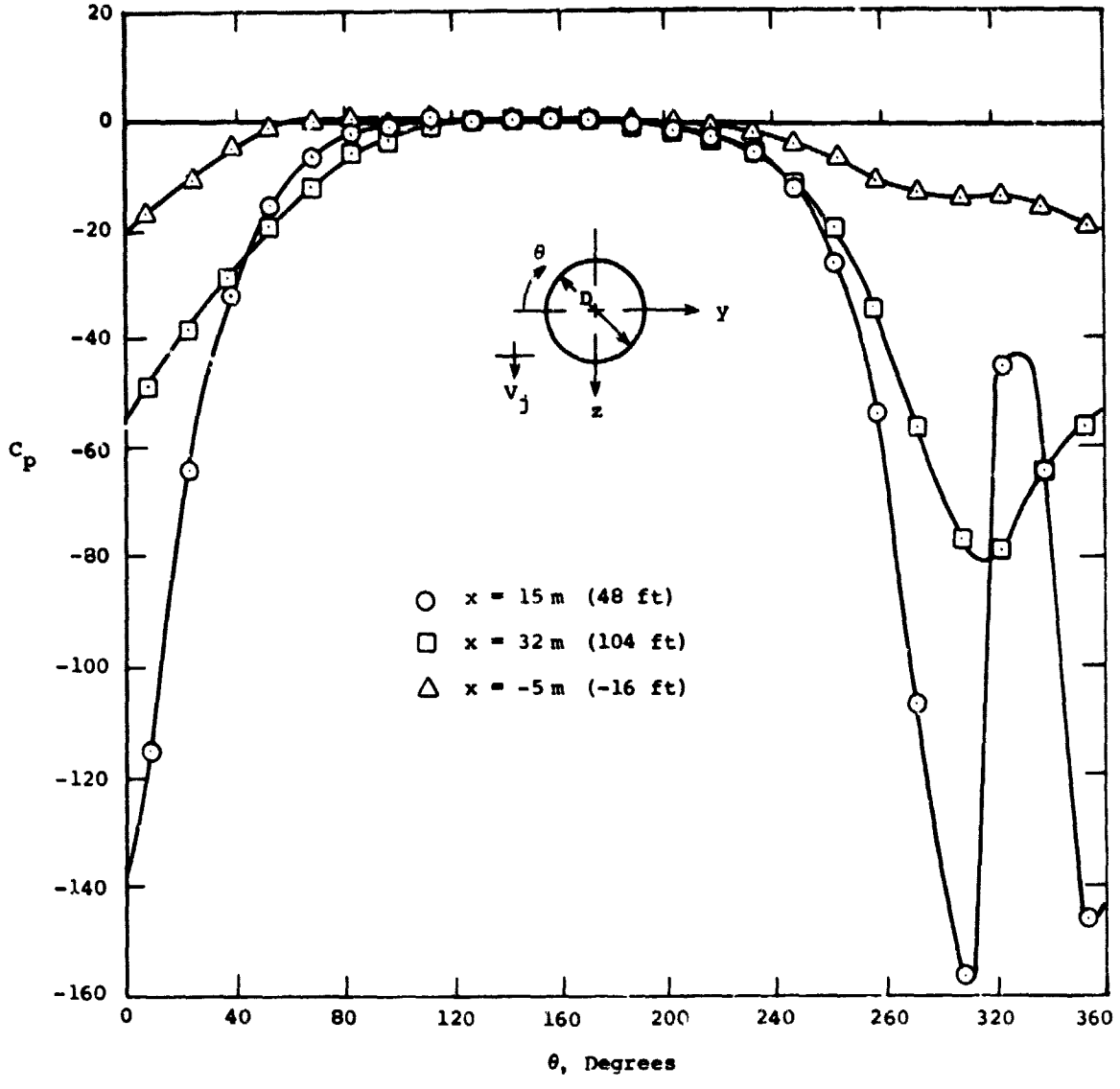

Figure 16.- Predicted circumferential pressure distributions on HLA hull in hover. T_4/S_R = 395 N/m² (8.26 psf).

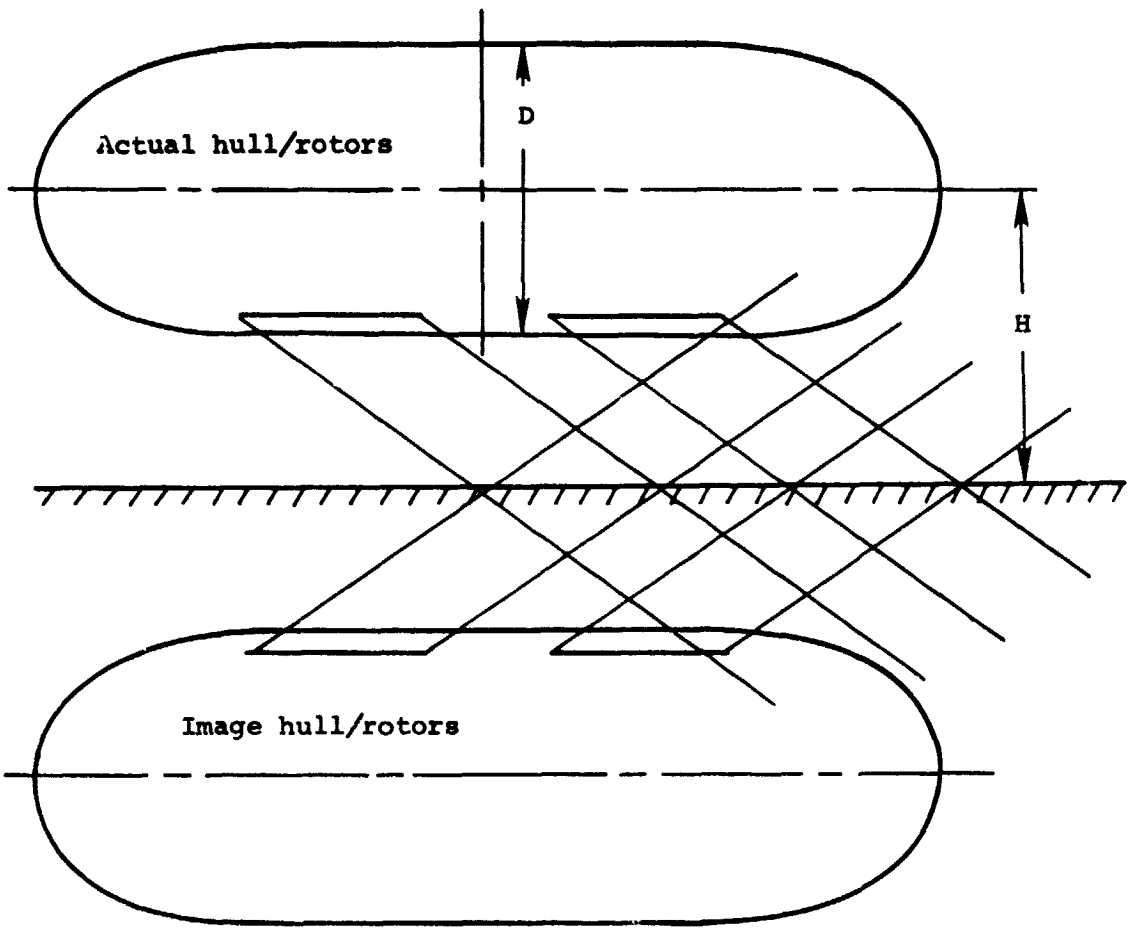

Figure 17.- Hull-wake configuration for HLA in-ground effect. H/D = 1.

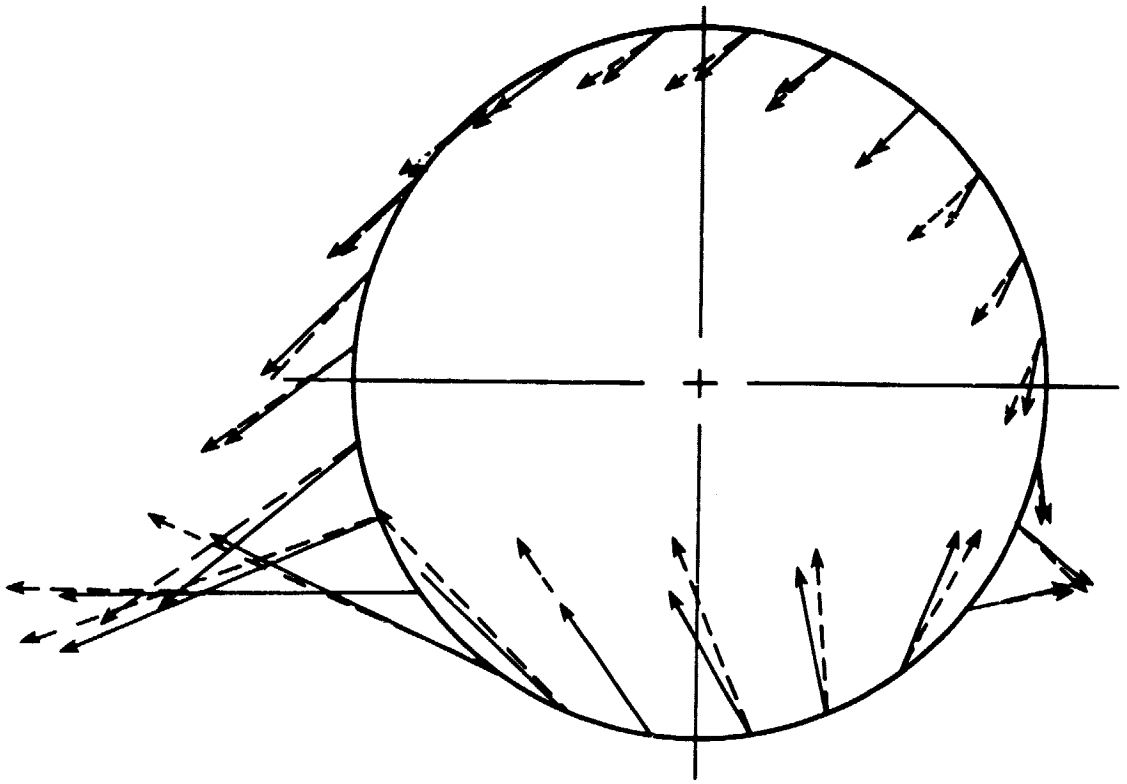

Solid vectors are in-ground effect

Dashed vectors are out-of-ground effect

Vector scale

$\longrightarrow$

$0.1\ V_\infty$

Figure 18.- Rotor-induced velocities on hull at z = 5 m (16 ft) for HLA in axial flow at 15.4 m/s (30 knots) in- and out-of-ground effect.

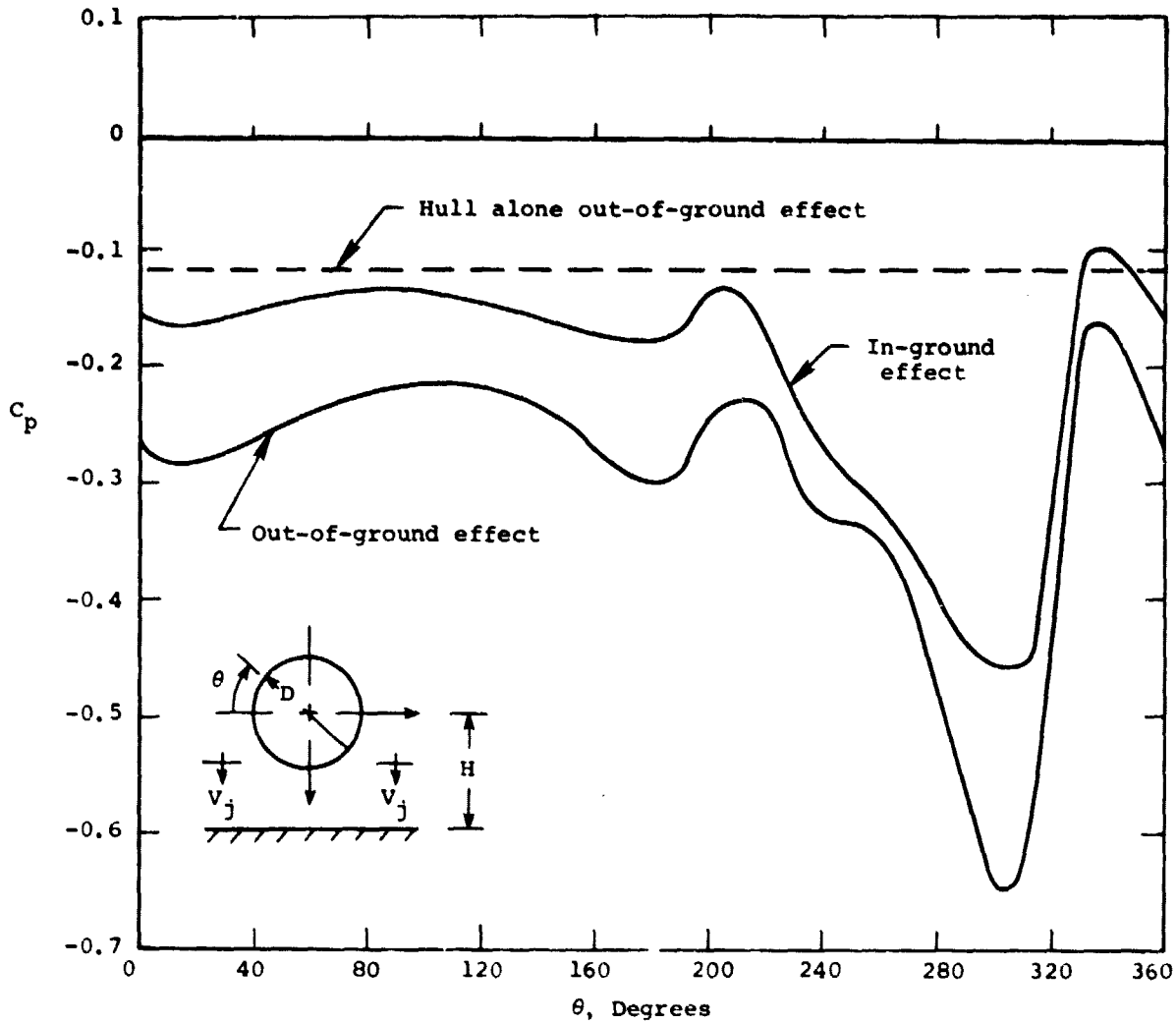

Figure 19.- Predicted hull pressure distributions for HLA in axial flow in- and out-of-ground effects. x = 5 m (16 ft).

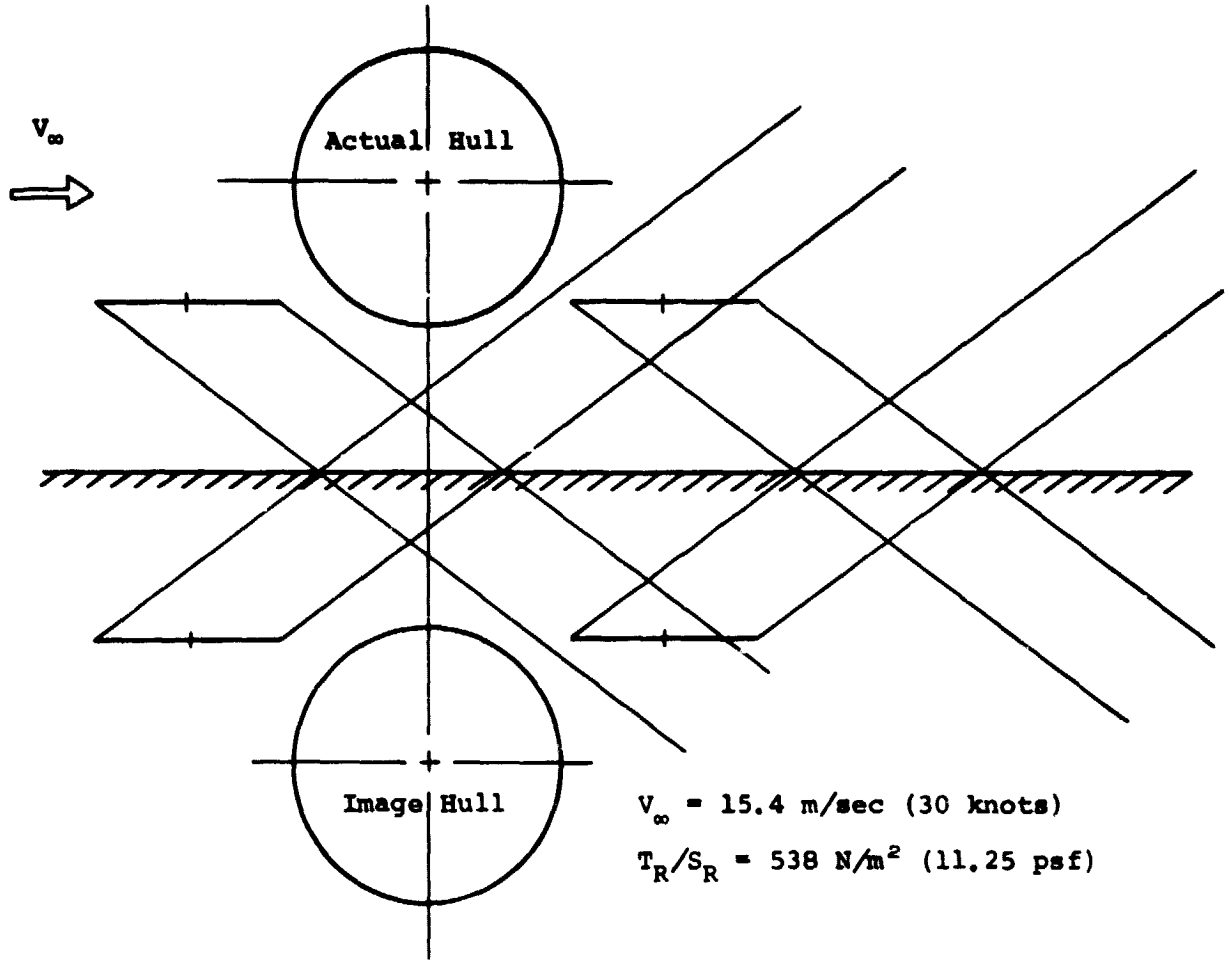

Figure 20.- Hull and rotor wake configuration for HLA in crossflow in-ground effect.

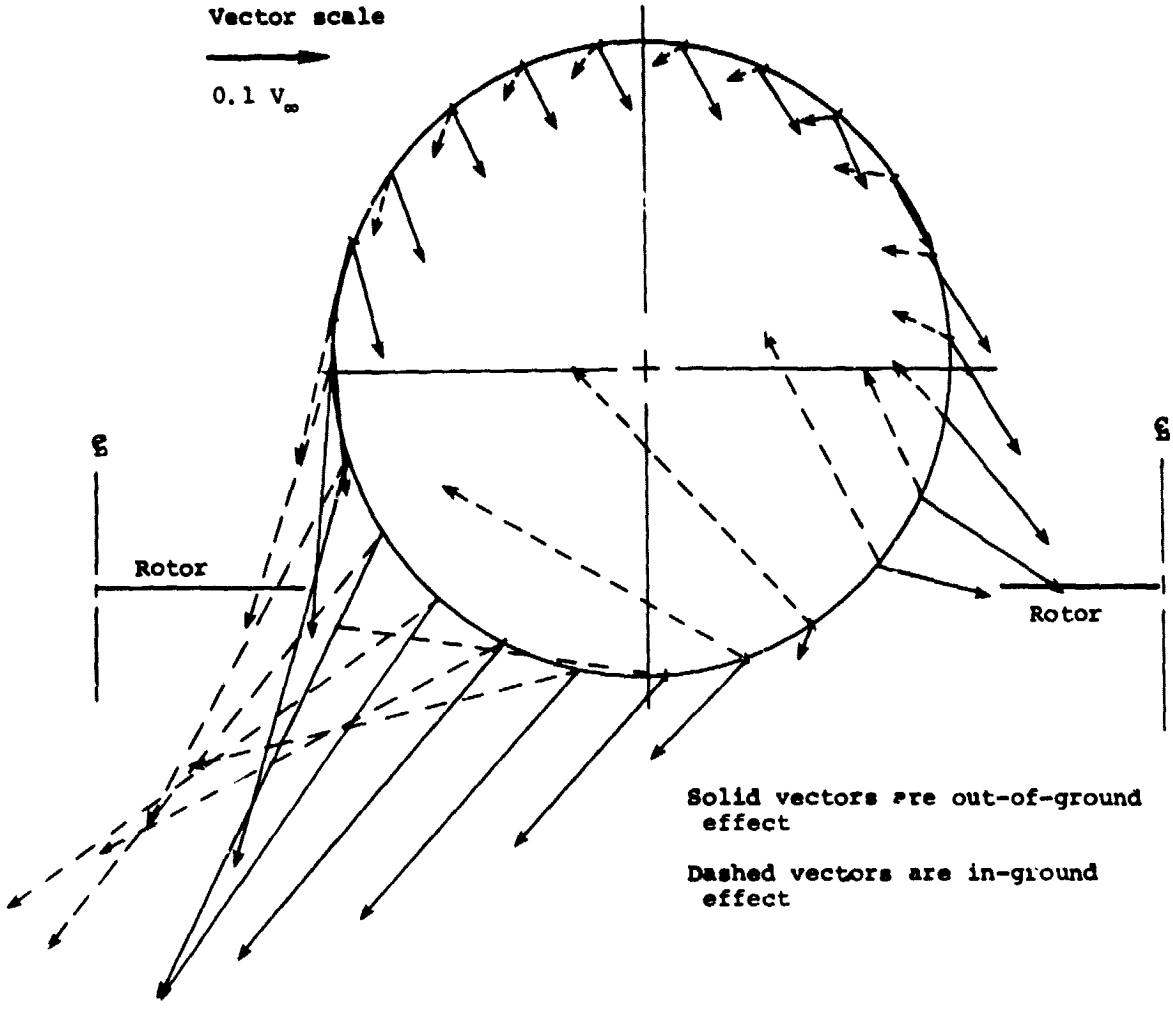

Figure 21.- Rotor-induced velocities on HLA hull in- and out-of-ground effect. $\alpha = 0$, $\beta = -90^\circ$. $x = -15$ m (-48 ft).

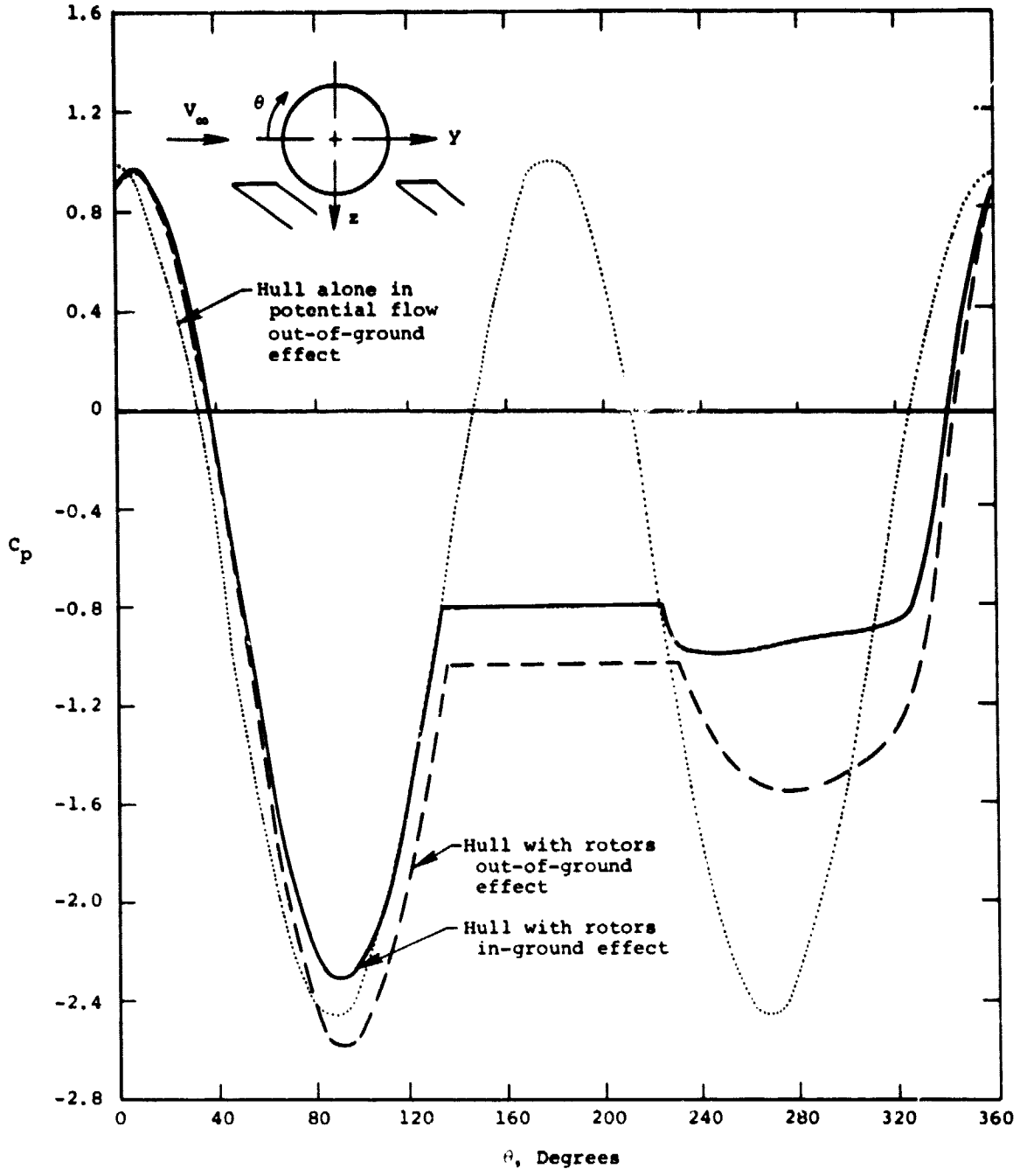

Figure 22.- Predicted hull pressure distribution at x = -15 m (-48 ft) for HLA at $\beta = -90^0$.
V = 15.4 m/sec (30 knots).
T_R/S_R = 478 N/m² (10 psf).

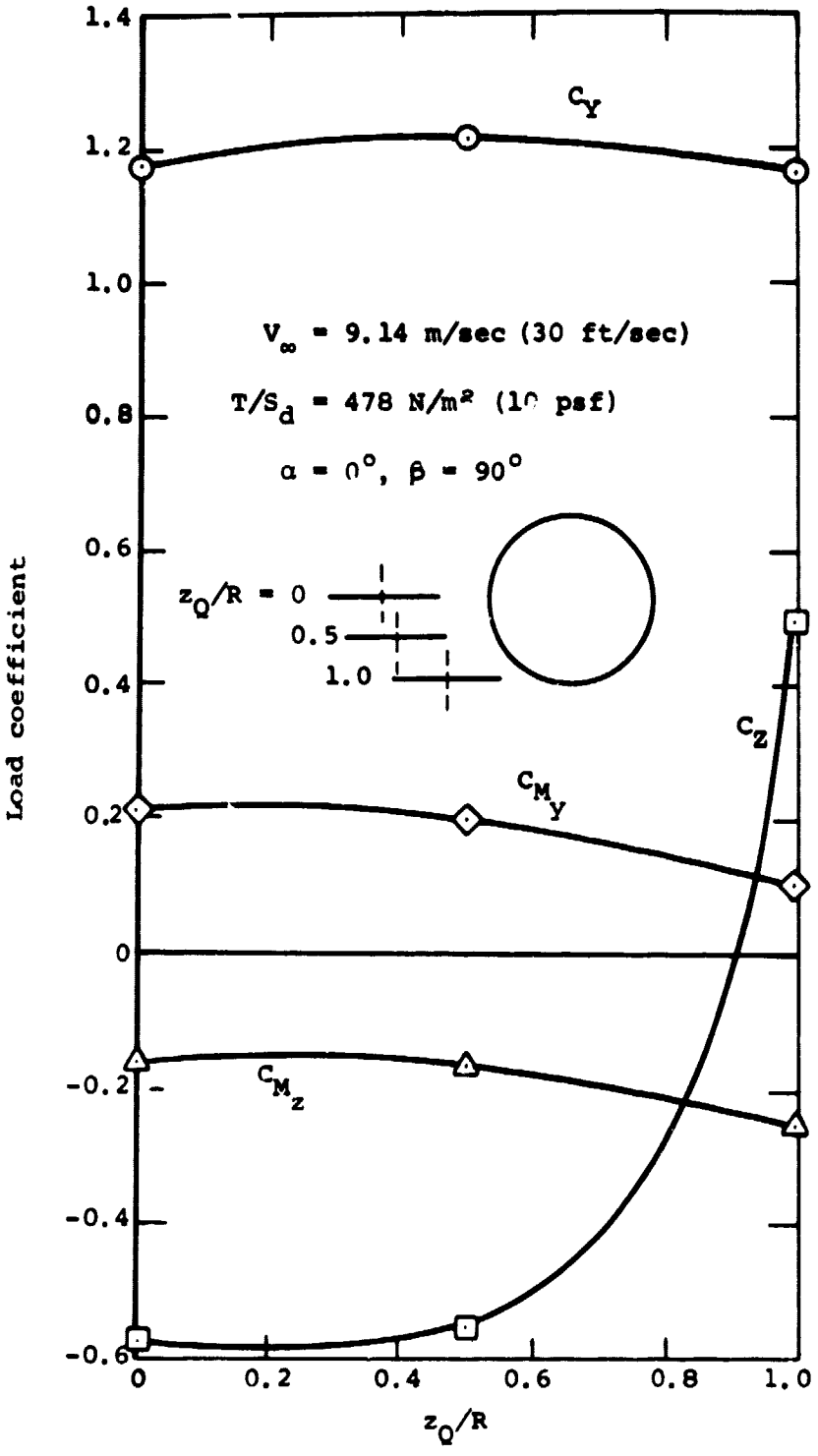

Figure 23.- Effect of rotor vertical placement on hull loads of HLA in crossflow.

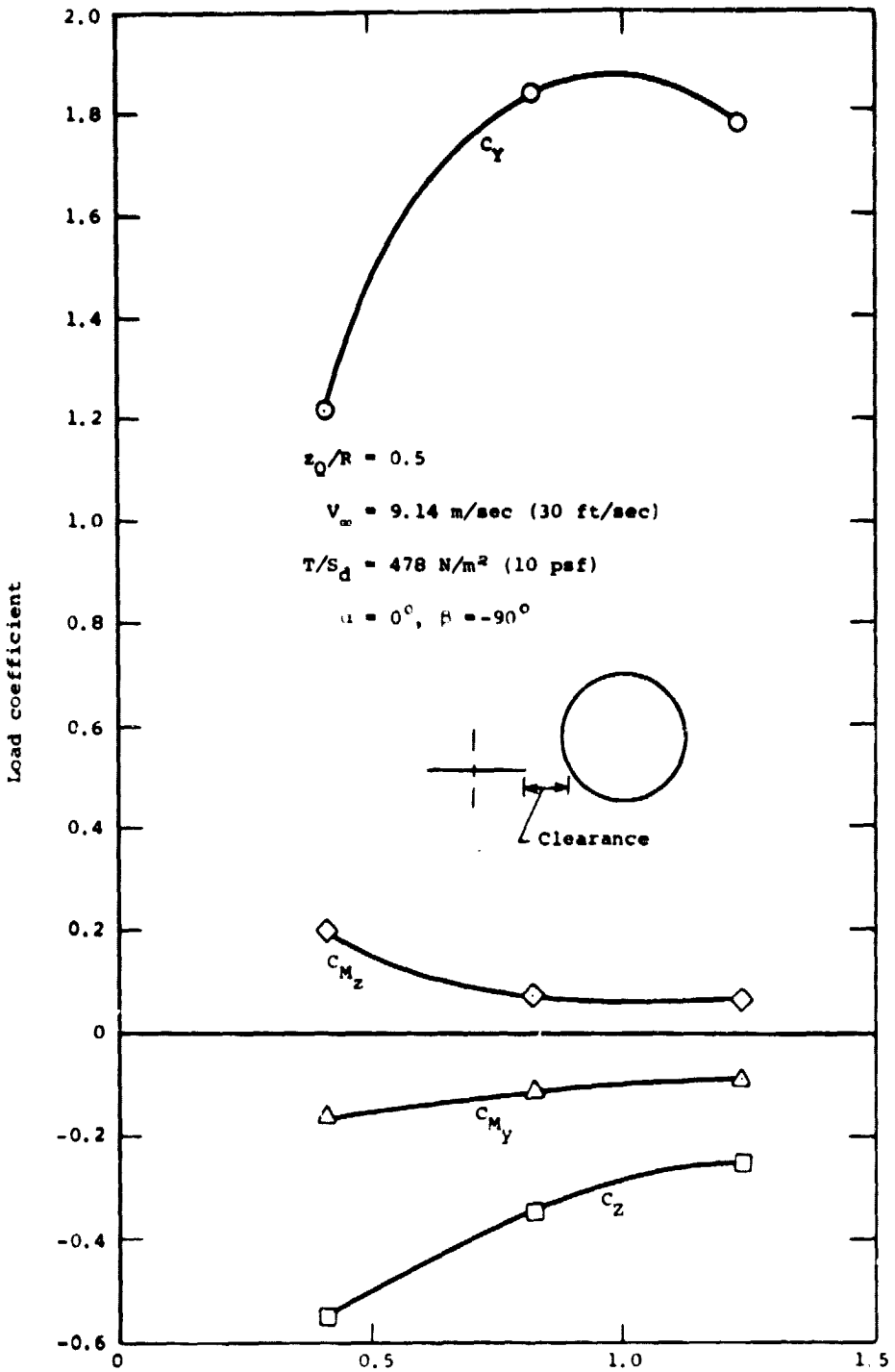

Figure 24.- Effect of rotor lateral clearance on hull loads for HLA in crossflow.